



UNIVERSITY OF LEEDS

Numerical Simulations of Dusty Colliding Wind Binaries



Joseph Eatson
University of Leeds
School of Physics and Astronomy

Submitted in accordance with the requirements for the degree of

Doctor of Philosophy

December, 2021

This thesis is dedicated to my Mum, without her help these past 26 years there's
no way I would have gotten this far.

I'll pay you back I promise.

Acknowledgements

If you're reading this ahead of time and wondering where you are, don't worry, I'm getting to you, just writing the thesis first!

I suppose a good place to start when thanking people in a thesis is to start with family. To my mum, when I asked you to for help funding my doctoral degree, you said yes, instantly, and without hesitation, considering all you have done and sacrificed for me throughout my life, your agreeing to help was another act of kindness that I can barely repay (trust me, I've done the numbers). You've been there for me, every step of the way, I could not ask for a more wonderful mum, and I hope I can make you proud.

I also owe a debt to my supervisor, Dr. Julian Pittard, you've gone above and beyond when it came to my supervision, you've solved bugs, found mistakes and gotten me out of a jam more times in this project than I can count. I'm still amazed how you can rattle off a paper or three from memory, when I've come into your office asking questions about a very specific part of my work, honestly, how do you do that? It's very impressive.

No good thesis¹ wouldn't be complete without a commitment to the authors friends. I first met some of you on the literal first day of my undergraduate degree, it's really quite incredible how you've all tolerated my nonsense for so long. From essentially forcing my way into Rob's house so I could cook some disastrous fried chicken, to playing *Super Smash Bros.* all night long on its release day, to watching trashy movies over the internet at the height of a global pandemic, these are moments I'll treasure for the rest of my life. In particular, those who are still in Leeds, Rob, Matt, Kelsie, Alex and Sam; as well as those who aren't, Martin, Caz, Andy, and Devon. Thank you all, for filling my life with joy this past decade. To my partner Pruthvi, I cannot stress how unlikely it is that the two of us even met - two people finding and falling for each other on the more esoteric circles of the internet is like two particles colliding in the tenuous interstellar medium, if you'll excuse the extremely trite metaphor. You've been loving, kind, helpful, and the most wonderful partner anyone could ask for. I truly am blessed to know you and love you.

I would also like to thank the fantastic team at Leeds' ARC High Performance Computing department, considering the bulk of this work involves many 3D numerical simulations my use of ARC 4's compute nodes can be described as somewhere

¹Though the quality of this one is debatable.

from “excessive” to “taking the piss”. I also apologise for running my earlier simulations on the login nodes for multiple days, I swear it was an accident.

I would also like to thank two figures from my formative years for inspiring me. The first is my 9th year Physics teacher, Isobel Why, who re-kindled my interest in the field, she was the finest teacher I ever had, turning me from an underachieving student to a keen and committed aspiring physicist. She truly had faith in all of her students, and pushed them far beyond what they thought themselves capable of. Whilst she left teaching shortly after that year, I will never forget her impact on my life and my work. Another is quite indirect, but still important, I would be amiss to thank Winchell “Nyrath” Chung, curator of the website [Atomic Rockets](#). Winchell’s work is perhaps one of the most complete and exhaustive archive of real life and fictional rocketry and space exploration resources - whilst I haven’t called on his work much during my career in astrophysics, I pored over this website when I was younger (perhaps reading it more thoroughly than any of my course textbooks). It was fascinating, insightful and inspiring not only to me, but thousands of readers; the number of projects, from hard SFF novellas to honest-to-goodness research proposals hinge on his tireless efforts to catalogue humankind’s exploration of space in both reality and fiction. I learned of his cancer diagnosis whilst writing this thesis, and it cut me to my core, without his work I don’t think I would have turned a fascination with space into a lifelong passion. Thank you so much, both of you, you may not realise it, you may not ever read this, but you changed my life.

Finally, I would like to thank Leandro Panizzon and his wife, Margarita, though Methylphenidate was originally synthesised by him to treat her low blood pressure, it also works quite well for dragging my attention-deficit disorder riddled brain through this PhD.

Abstract

CONTENTS

1	Introduction & Motivation	1
1.1	Dust Formation in Colliding Wind Binary Systems	2
1.2	Motivation	2
1.3	Thesis Structure	2
2	Background	3
2.1	Early-Type Stars	4
2.1.1	OB-type stars	4
2.1.2	Wolf-Rayet stars	7
2.2	Stellar Winds	8
2.2.1	Stellar winds in low mass stars	9
2.2.2	Stellar winds in high mass stars	9
2.2.3	The CAK formalism	12
2.3	Interstellar Dust	12
2.3.1	The importance of interstellar dust	12
2.3.2	Interstellar dust in massive star systems	12
2.3.3	Radiation processes in interstellar dust	12
2.4	Colliding Wind Binary Systems	12
2.4.1	The Wind Collision Region	13
2.4.2	Cooling in the WCR	14
2.4.3	Dust formation in CWB systems	17
2.4.4	Important WCd systems	17
2.4.5	Contemporary research in extragalactic low-metallicity WCd systems . .	17

CONTENTS

3 Methodology & Numerical Simulation	19
3.1 A Short History of Numerical simulations	20
3.2 The Purpose of Numerical Simulations	20
3.3 The Mathematics of Numerical Simulations	20
3.4 Computational Hydrodynamics	20
3.4.1 Comparison of hydrodynamical methods	20
3.5 The Athena++ Hydrodynamical code	20
3.6 Mesh Refinement	20
3.7 Visualisation	22
3.8 Simulating CWB systems	23
3.8.1 Assumptions	23
3.9 Cooling in numerical simulations	23
3.9.1 Plasma cooling	24
3.9.2 Dust cooling	24
3.9.3 Implementation	30
3.10 The BODMAS Adverted Scalar Dust Model	34
3.10.1 BODMAS features	35
3.10.2 Contemporary dust Models	35
3.10.3 Implementation	36
3.10.4 Future dust models	36
4 A Parameter Space Exploration of Dust Formation	39
4.1 Introduction	40
4.2 Methodology	42
4.2.1 Gas and dust cooling	45
4.2.2 Numerical modelling of dust through advected scalars	49
4.3 Model Parameters	50
4.3.1 Cooling mechanisms	51
4.3.2 Wind momentum ratio	52
4.3.3 Separation distance	52
4.3.4 Data collection	54
4.4 Results	54
4.4.1 Radiative processes	54
4.4.2 Mass loss rate variation	58

CONTENTS

4.4.3	Terminal velocity variation	60
4.4.4	Separation variation	65
4.5	Conclusions	67
4.5.1	Dust formation sensitivity	67
4.5.2	Radiative inhibition and its influence on eccentric WCd systems	67
4.5.3	Wind mixing within the WCR	68
4.6	Summary and Conclusions	69
5	Hydrodynamical Simulations of WCd Systems	71
5.1	Introduction	72
5.2	Methodology	73
5.2.1	Hydrodynamics	73
5.2.2	Dust model and cooling	75
5.2.3	Simulated systems	76
5.2.4	Radiative transfer modelling	78
6	Influence of Wind Velocity on Dust Formation	81
6.1	Introduction	82
6.2	Methodology	82
6.3	Model Parameters	82
6.4	Results	82
7	Final Notes and Conclusions	85
7.1	Conclusions	86
7.1.1	Causes of dust formation in WCB systems	86
7.1.2	The role of eccentricity in dust formation	86
7.2	Future Study	86
7.2.1	More complex models	86
7.2.2	Further simulations of observed systems	86
7.2.3	Radiative transfer	86
7.2.4	WR+WR systems	86
7.2.5	Next generation telescopes	86
7.3	Other Observations	86
7.3.1	<i>How I Learned to Stop Worrying and Love Numerics</i>	86
7.3.2	Join the physics department, see the world	86

CONTENTS

7.3.3	Paul Erdős was probably onto something	86
7.3.4	Carinae Strain: PhD research in a time of pandemic	86
7.3.5	WR 104 as a local GRB candidate	86
A	Astrophysical Shocks	87
B	Software Carpentry	89
B.1	Amdahl’s Law	90
B.2	Version Control	90
	References	91

LIST OF FIGURES

2.1	Planck's law radiance comparison with resonance lines	10
2.2	M1-67 nebula around WR 124	11
2.3	ρ_w comparison of main sequence winds	13
2.4	WC & solar abundance plasma cooling curves	15
2.5	Dust cooling vs. plasma cooling	16
2.6	H_{el} and H_{coll} comparison	18
3.1	Adaptive mesh refinement comparison	21
3.2	h_e integration accuracy comparison	25
3.3	Dust lookup table methods comparison	27
3.4	Electron transparency method accuracy - h_e	28
3.5	Electron transparency method accuracy - H_{el}/H_{coll}	29
3.6	Electron transparency method accuracy - Λ_d	29
3.7	Ionisation fraction for OB and WC stars	31
3.8	Cooling sub-step method evolution comparison	32
3.9	Cooling sub-step method accuracy comparison	34
3.10	Hendrix et al. (2016) synthetic astronomy	38
4.1	Static mesh refinement example	44
4.2	WR and OB $\Lambda(T)$ cooling curves	46
4.3	OB and WR electron-ion ratios	47
4.4	Comparison of electron transparency methods.	48
4.5	Comparison of threshold values for over-density method	55
4.6	Comparison of dust and plasma cooling rates in post-shock environment	56
4.7	Instabilities due to cooling	57

LIST OF FIGURES

4.8	Comparison of dust formation rates with cooling methods	57
4.11	<code>Baseline</code> simulation z , full extent	60
4.12	Dust production rate for simulations varying mass loss rate	61
4.14	Dust density comparison of terminal velocity varying systems	62
4.15	OB terminal velocity wind dust comparison	64
4.16	Wind colour comparison of $\eta = 0.04$ winds	64
4.19	Dust formation rate vs. binary separation distance	66
4.20	Stagnation point wind velocity	69
4.21	Wind mixing due to radiative methods	70
5.1	Orbital path comparison	78
5.2	χ change over system orbit	79

LIST OF TABLES

2.1	Stellar wind comparison	12
2.2	Cooling processes at various temperature ranges	14
3.1	Dust cooling calculation comparison	30
3.2	Cooling method accuracy comparison	35
3.3	Cooling method performance comparison	35
4.1	Abundances used for OB and WR stars	46
4.2	Wind properties of the baseline system.	51
4.3	Baseline system orbital properties.	51
4.4	Cooling series simulation parameters	51
4.5	Mass loss rate series wind parameters	52
4.6	Terminal velocity series wind parameters	53
4.7	Parameters of simulations varying separation distance.	53
5.1	Wind properties of systems simulated in this paper.	77
5.2	Orbital properties of systems simulated in this paper.	77
6.1	WR parameters	83
6.2	OB parameters	84

Abbreviations

List of common abbreviations, if an abbreviation is important enough to warrant a section in this thesis, the section will be referenced.

BODMAS	Binary Orbit Dust Model with Accretion and Sputtering	Section 3.10
CWB	Colliding Wind Binary	Section 2.1.1
GMC	Giant Molecular Cloud	Section 2.1.1
LBV	Luminous Blue Variable	Section 2.1.1
OB	O or B type star	Section 2.1.1
RSG	Red Supergiant	Section 2.1.1
WC	WR Carbon Phase	Section 2.1.2
WCd	Dust forming WC star	Section 2.4.3
WCR	Wind Collision Region	Section 2.4.1
WN	WR Nitrogen Phase	Section 2.1.2
WO	WR Oxygen Phase	Section 2.1.2
WR	Wolf-Rayet	Section 2.1.2

Common Symbols

List of common symbols, if symbol requires a derivation, the appropriate equation within this thesis will be referenced. If the symbol is a unit, the value in CGS units will be provided instead.

a	Grain radius	
C	Courant-Friedrichs-Lowy condition	
h_e	Electron transparency	Section 2.4.2
H_{coll}	Grain heating rate due to ions	
H_{el}	Grain heating rate due to electrons	
L_*	Stellar luminosity	
M_*	Stellar mass	
\dot{M}	Mass loss rate	
v_∞	Wind terminal velocity	
z	Dust-to-gas mass ratio	
β	Electron ion ratio	
η	Wind momentum ratio	
$\Lambda(T)$	Plasma Cooling function	
$\Lambda_d(h, a, T)$	Dust cooling function	
ξ	Grain sticking efficiency	
θ_c	WCR conic opening angle	Equation 2.10
τ_{KH}	Kelvin-Helmholtz timescale	Equation 2.1a
τ_{ff}	Free-fall timescale	Equation 2.1b
τ_{cool}	Cooling timescale	Equation 2.11a
τ_{esc}	Escape timescale	Equation 2.11b
μ	Mean molecular mass	
κ	Sub-timestep fraction	3.10
χ	Cooling parameter	Equation 2.12

M_{\odot}	Solar mass	1.988×10^{33} g
$M_{\odot} \text{ yr}^{-1}$	Solar mass per year	6.301×10^{25} g s $^{-1}$
L_{\odot}	Solar Luminosity	3.828×10^{33} erg s $^{-1}$
AU	Astronomical Unit	1.496×10^{13} cm
pc	Parsec	3.086×10^{18} cm
“warm”	Warm temperature regime	Between 10^4 and 10^5 K, personally

CHAPTER 1

Introduction & Motivation

1. INTRODUCTION & MOTIVATION

1.1 Dust Formation in Colliding Wind Binary Systems

1.2 Motivation

1.3 Thesis Structure

CHAPTER 2

Background

2. BACKGROUND

2.1 Early-Type Stars

The term Early-type stars is quite possibly the epitome of bad naming conventions in astrophysics, it's a very old term, coming from the dawn of astrophysics itself, quite opaque as to what it means, and also by definition *completely wrong*. In fact it is one of the most wrong pieces of terminology I can think of.¹ The first generation of astrophysicists found themselves asking very important questions such as “what even *are* stars” and “what possible mechanism can allow a star to burn for so long?” Each of these questions was rather pressing for the burgeoning field, and the scientific community was aching for an answer.

Of course, like all pressing questions of the 19th century, it fell to Lord Kelvin to provide a convincing but incorrect answer. Kelvin assumed that gravitational collapse was the mechanism for a stars long-term heating, with younger, “early” type stars shining the brightest. Not only was the mechanism incorrect, but typically older main sequence stars are more luminous than their younger counterparts of a similar mass! However, as is the case with astrophysical terminology, the term stuck, to the confusion of many young astrophysicists.

Instead, we now know that stars produce their energy through fusion. These reactions vary from sub-stellar deuterium and lithium burning, to main sequence p-p & CNO hydrogen burning processes, and finally to the triple- α and other exotic fusion processes for evolved massive stars. The more massive the star the greater the internal pressure, allowing for more exotic fusion processes. The bigger a star, the greater the core pressure and temperature, as all fusion reactions are highly dependent on temperature, stars with only a few dozen solar masses are thousands of times more luminous than our sun, but only live a fraction of the time (Carroll & Ostlie, 2014).

2.1.1 OB-type stars

And with that we shift our gaze to high-mass stars, with the most massive of all being the O and B type stars, these are extremely luminous ($\sim 10^4 L_\odot$), and relatively short lived (~ 10 Myr) stars. The age-old adage of a candle burning twice as bright lasting half as long applies to our studies of the cosmos, but it is more apt to compare a candle and a stick of dynamite when considering stars on opposing ends of the Harvard classification system.

The most common formation mechanism of stars is through the collapse of a giant molecular

¹Aside from astrophysicists calling something “warm”, of course. That can quite literally mean anything from 10 to 10,000 Kelvin, depending on who you ask, what they’re writing about, or how they’re feeling at that particular moment. In fact, I’ll probably end up falling into this same trap somewhere in this thesis as well!

2.1 Early-Type Stars

cloud¹, an enormous cool cloud many parsecs across with a mass of around $10^4 M_\odot$. As this GMC collapses and radiates energy, lowering the radius of thermostatic equilibrium for the cloud, as collapsing progresses the cloud fragments into many smaller regions with a critical density, capable of collapsing further, forming a star. The collapse of a GMC can be described with a series of timescale. First, the Kelvin-Helmholtz timescale, τ_{KH} , which describes the timescale required for the radiating cloud to collapse. The second important timescale is the free-fall timescale, τ_{ff} , which is the time taken for a cloud to collapse. These timescales are described by the following equations:

$$\tau_{KH} \approx \frac{GM_*^2}{R_*L_*}, \quad (2.1a)$$

$$\tau_{ff} = \sqrt{\frac{3\pi}{32G\rho}}, \quad (2.1b)$$

where M_* is the protostellar mass, R_* is the protostellar radius, L_* is the protostellar luminosity, and ρ is the mean density of the collapsing cloud (Ward-Thompson & Whitworth, 2011).

Perhaps the most important distinction between massive star formation and its better understood counterpart is as a young protostar approaches the main sequence, the KH timescale is less than the free-fall timescale, meaning the material at the center of the collapsing cloud begins fusion while the bulk of core has collapsed onto the site of the future star. This burgeoning star begins to drive the weakly gravitationally coupled collapsing material away due to its sheer luminosity, driving this material outwards, causing it to accrete and shock material within the GMC.

Another important consideration is the role of angular momentum as the star collapses. The particularly massive cloud involved in massive star formation is more prone to fragmentation, meaning that massive stars typically form with an orbital partner, whilst approximately 2/3^{rds} of low-mass stars are part of a binary or multiple system, this value is near-total. As such, the environment within an OB association after star formation consists of numerous young stars in tightly-knit groups disrupting the entire local area.²

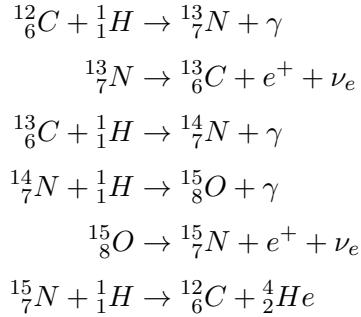
Above a stellar mass of $1.3M_\odot$ pressures and temperatures within a stellar core favour the fusion of hydrogen into helium through the catalytic CNO cycle, instead of the more direct p-p

¹GMC

²This is a bit like living in Headingley, Hyde Park, or any other area with lots of Undergraduates.

2. BACKGROUND

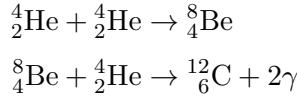
fusion process.



The reaction rate of CNO rises much faster, resulting in a convective core, surrounded by a radiative envelope (Salaris & Cassisi, 2005). This is the driving force behind the incredible luminosities of an OB star as it hurtles along the main sequence.

Unfortunately for massive stars, pesky fundamental laws such as the conservation of energy come into play. With only an order of magnitude or two of additional mass more than our sun and shining 10^4 times as brightly, this curtails the life of the brightest stars to lifespans not much more than 10^7 years. If we define a galactic year as the time it takes for a star to orbit the Milky Way, these poor stars don't even make it to their first birthdays, which is quite sad really.¹

As the available hydrogen begins to become depleted, the lowering reaction rates force the star to shrink, this raises the internal temperature until the core begins to burn helium through the triple- α process:



The sudden spike in energy radiating from the core shifts the calculus of hydrostatic equilibrium in the favour of outward forces, causing the star to rapidly expand in the form of a Red Supergiant or Luminous Blue Variable (Ryan & Norton, 2010). During this phase the energy output of the star is even greater, with a timescale of $\sim 10^6$ years, this is only temporarily prolonging the life of the star, which will inevitably begin burning heavier and heavier elements,

¹Continuing this analogy our sun can drink, might have voted if they felt like it, and may be racking up vast quantities of student debt.

faster and faster. Once the star starts producing iron its fate is sealed, the star stops fusing, and collapses, annihilating itself in the form of a supernova and leaving behind a remnant of its core in the form of a neutron star or black hole (Ward-Thompson & Whitworth, 2011).

Whilst the stars end is as inevitable as it is violent, the intermediate stage as the star leaves the main sequence is in itself extremely interesting, and for the context of this thesis, no product of this stage is more interesting than the Wolf-Rayet.

2.1.2 Wolf-Rayet stars

As we now know, Wolf-Rayets¹ are evolved forms of O-type stars, and are a short lived component of the life-cycle of massive stars, typically lasting for around 5×10^5 years (Crowther, 2007). Despite this relatively transient length of this stage, the influence of a WR star on its local medium is extremely outsized. WR stars in particular are known for having dense, fast winds, typically between 2 and 3 orders of magnitude than their main sequence O-type progenitors, with mass loss rates on the order of $10^{-5} M_{\odot} \text{ yr}^{-1}$ and wind velocities of $1.5 \times 10^3 \text{ km s}^{-1}$. This extremely dense wind is driven by the highly energetic helium burning core, which is luminous enough as to drive away the outer layers of the stars envelope, exposing the core. The observed spectroscopic lines are due to heating of the envelope from the core, which is enriched with by-products of hydrogen and helium burning, the lack of hydrogen lines is due to the stars evolved nature, as all the hydrogen has been burned, there is simply nothing left to observe!

Wolf-Rayet stars can be subcategorised through spectroscopic observation, which indicates enrichment in a particular element, the 3 major sub-types, WN, WC and WO are defined by their strong nitrogen, carbon and oxygen lines respectively. The important distinction between WN and WC/WO stars is that WN stars are enriched through hydrogen burning, whilst WC and WO are enriched through the by-products of helium burning (Vink, 2015).

As a Wolf-Rayet continues to lose its envelope, additional products of fusion processes are dredged up from the centre of the star. In the case of the WN sub-type, the broad nitrogen lines correspond to the outer layer of the envelope, enriched through the CNO process; after this outer envelope is cast off, the remainder of the envelope exhibits carbon and oxygen lines, indicating enrichment from the triple- α process. Finally, the star evolves further and the innermost region of the envelope is revealed, observed as the strong oxygen lines of a WO sub-type (Neugent & Massey, 2019; Oswalt & Barstow, 2013).

As an O-type star transitions to a Wolf-Rayet, it typically undergoes an intermediary LBV

¹Abbreviated to WR.

2. BACKGROUND

or RSG stage as helium burning begins, this is mass dependent, with the various transitional states described by Crowther, 2007:

$$O \rightarrow LBV/RSG \rightarrow WN(H\text{-poor}) \rightarrow WC \rightarrow SN\ 1b, \text{ for } 25 M_{\odot} < M_{WR} < 40 M_{\odot}$$

$$O \rightarrow LBV \rightarrow WN(H\text{-poor}) \rightarrow WC \rightarrow SN\ 1c, \text{ for } 40 M_{\odot} < M_{WR} < 75 M_{\odot}$$

$$O \rightarrow WN(H\text{-rich}) \rightarrow LBV \rightarrow WN(H\text{-poor}) \rightarrow WC \rightarrow SN\ 1c, \text{ for } M_{WR} > 75 M_{\odot}$$

Wolf-Rayet stars are important in the context of this work due to their outsized influence within a WR+OB binary pair. The WR component of a WR+OB binary has an outsized contribution in returning material to the ISM, whilst also dominating the dynamics of the system, with their winds completely overpowering those of their O-type neighbours. In some cases, the dense, fast wind from the WR can collide with the much more tenuous wind from its partner, forming a strong shock, and a variety of fascinating effects. However, I wouldn't want to spoil too much too soon, but you can skip ahead to section 2.4, where this phenomena is covered in more detail.

2.2 Stellar Winds

Stellar winds have already been discussed to some extent in the previous section, however, due to the significance of winds within this body of work, further detailing of winds must be discussed to gain a better understanding of the dynamics of Colliding Wind Binary systems. This section will cover in brief the study of stellar winds, particularly driving mechanisms from low and high mass stars.

The study of stellar winds is of course, rather hard from our vantage point on Earth, as direct observation of a non-stellar solar wind is difficult, and sampling of the winds themselves significantly more difficult than that due to the inconvenient distances involved in interstellar travel. Because of this, extrasolar wind properties are derived from spectrography, with velocities derived through Doppler shift. The important parameters to consider in a wind, especially for this thesis, is the mass loss rate, \dot{M} , the wind terminal velocity, v^{∞} and the abundances within the wind.

$$\frac{dM}{dt} = 4\pi\rho(\mathbf{r})v(\mathbf{r})\mathbf{r}^2, \quad (2.5)$$

$$\rho_w = \frac{\dot{M}}{4\pi v^\infty r^2}, \quad (2.6)$$

This section will cover the different driving mechanisms winds from low and high mass stars, the typical wind parameters and driving mechanisms are broken down in table 2.1.

2.2.1 Stellar winds in low mass stars

Low mass stellar main sequence stellar winds are quite paltry for an astrophysical phenomenon, the sun, for instance, drives thin, comparatively slow winds, with a mass loss rate of $\sim 10^{-14} M_\odot \text{ yr}^{-1}$ and a terminal velocity of 400 km s^{-1} . The mechanism behind this is gas pressure from coronal heating, with outward pressure driving gas within stellar atmosphere away from the star, this results in a transonic wind that quickly reaches its terminal velocity as the coronal temperature and subsequent pressure quickly drops off.

As a low mass star exits the main sequence, ballooning in size to become a red giant, the density of the stellar wind increases dramatically.

As dust condenses in the upper atmosphere of the red giant, these grains can readily adsorb photons, utilising radiation pressure to be driven away from the more luminous giant star, easily achieving escape velocity against the low surface gravity of the red giant. Gas is also driven away, coupled to the dust, this provides an efficient form of momentum transfer, allowing for an extremely dense albeit slow stellar wind

2.2.2 Stellar winds in high mass stars

In the same way that high-mass stars are many orders of magnitude brighter than their low mass counterparts despite a comparatively low increase in mass, the same can be said of the density of stellar wind. A main sequence OB star typically has a mass loss rate of $10^8 M_\odot \text{ yr}^{-1}$, 6 orders of magnitude higher than a solar mass star. This discrepancy in wind density cannot be explained by stronger coronal heating, in fact, the lack of a convective envelope ensures that coronal heating is not even feasible as a driving method! Instead we must look towards the higher luminosities that massive stars exhibit to find a suitable mechanism.

Simple radiation pressure from these stars would not be enough to explain the observed dense, highly supersonic winds emanating from these massive stars.

Resonance lines were also considered, a photon with an energy equal to the excitation energy of an ion is absorbed by that ion, gaining the momentum of this ion. The ion subsequently de-excites over a timescale on the order of 10^{-8} s , emitting a photon at a random angle relative

2. BACKGROUND

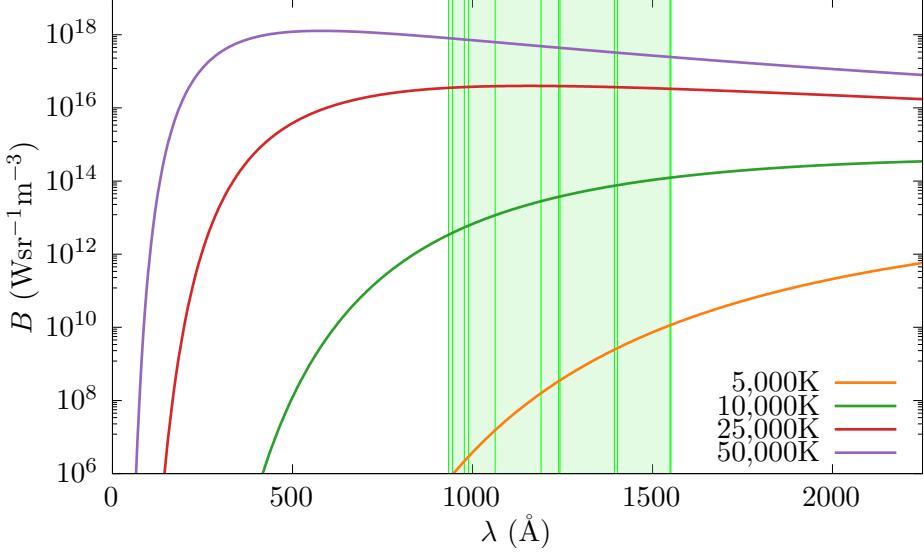


Figure 2.1: Spectral radiance against wavelength for black body objects at various effective temperatures, T_{eff} , a series of wavelengths corresponding with important resonance lines in table 1 of Lucy and Solomon, 1970 have been included. As temperature increases the spectral radiance at resonance line wavelengths dramatically increases, with a minimum of 6 orders of magnitude difference between the effective temperatures of a solar equivalent main sequence star and an O-type main sequence or Wolf-Rayet star.

to the radial direction, α . The resultant change in radial velocity, Δv_r , for the adsorption of a photon at the resonance frequency ν_0 is

$$\Delta v_r = v_r'' - v_r = \frac{\hbar\nu_0}{mc}(1 - \cos\alpha), \quad (2.7)$$

where v_r'' is the radial velocity after the absorption and emission events, and m is the ion mass. These ions are accelerated away from the star, along with the rest of the stellar wind which is coupled through Coulomb forces. The opacity of such resonance lines can be up to six orders of magnitude larger than the opacity of a Thomson scattering event (Lamers & Cassinelli, 1999). Additionally, this effect is not observed in low-mass stars, whose spectra typically peak in the visible light, while resonance lines typically have energies equivalent to UV photons (figure 2.1). O-type stars and Wolf-Rayets, however, emit much of their radiation within the UV range.

Early computations involving resonance lines from Lucy and Solomon, 1970 provided a more

2.2 Stellar Winds

reasonable mass loss rate calculation, but were still off by approximately two orders of magnitude. Building off of the work by Lucy & Solomon, a vital paper in the solidification of radiative lines as the main driving mechanism behind massive star outflows was produced by Castor, Abbott and Klein¹. The CAK formalism calculated reasonably close wind velocities, while being accurate to within a factor of 3 for mass loss rates (Castor et al., 1975). Further work allowed for more accurate computations of the line driving effect, such as the mCAK prescription, the Sobolev approximation and the finite disk correction factor (Pauldrach et al., 1986).

As previously mentioned, evolved massive stars progress into a helium burning WR phase, at this point, mass loss rates due to radiative line driving are extreme, in the order of $10^{-5} M_{\odot} \text{ yr}^{-1}$. This outsized influence on the local medium can be seen in the production of ejecta nebula, such as M1-67 produced by WR 124 (figure 2.2).



Figure 2.2: Reduced Hubble WFPC2 instrument data of the WN star WR 124, its extreme mass loss is currently producing an ejecta nebula, M1-67 (Marchenko et al., 2010).

¹Hereafter abbreviated as CAK.

2. BACKGROUND

Star	\dot{M}	v_∞	Mechanism
	$M_\odot \text{ yr}^{-1}$	km s^{-1}	
Sun	10^{-14}	400	Thermal heating
Pre Main Sequence	$10^{-4} - 10^{-7}$	200-500	Rotation & magnetic fields
Red Giant	$10^{-7} - 10^{-9}$	30	Radiation pressure on dust grains
OB Star	$10^{-7} - 10^{-8}$	2500	Radiation pressure & line driving
Wolf-Rayet	10^{-5}	1500	Radiation pressure & line driving

Table 2.1: Comparison winds emitted from various types of star.

2.2.3 The CAK formalism

2.3 Interstellar Dust

2.3.1 The importance of interstellar dust

2.3.2 Interstellar dust in massive star systems

2.3.3 Radiation processes in interstellar dust

2.4 Colliding Wind Binary Systems

Colliding Wind Binaries¹, in opposition to all known laws of astrophysical nomenclature, is a easy to understand term - it is a binary system where stellar winds from the member stars undergoing collision. Unfortunately, the simplicity of the systems ends here, CWB systems are extremely complex and poorly understood as they are difficult environments to observe or simulate.

Early observations beyond visual spectrum led to the discovery of many new astrophysical phenomena, one such discovery were extremely bright persistent thermal x-ray sources, with x-ray The first classification and analysis of Colliding Wind Binary systems were independently performed by Prilutskii and Usov, 1976 and Cherepashchuk, 1976, these systems were found to contain a close binary system, consisting of an evolved WR star and an OB counterpart, as their winds collide, a strong shock forms, heating the winds to temperatures in the order of 10^8 K in the immediate post-shock environment, these extreme temperatures and the large quantity of shocked material accounted for the extremely bright thermal x-ray emission. The evidence was

¹Abbreviated to CWBs.

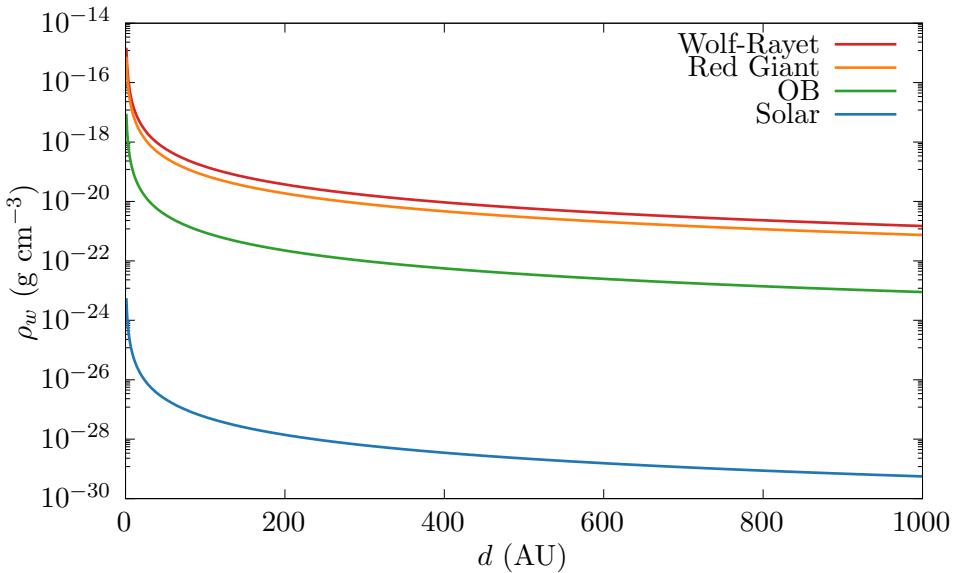


Figure 2.3: Comparison of the densities of various main sequence winds using the parameters specified in table 2.1, wind densities are estimated using the smooth wind approximation described in equation 2.6.

further compounded as the variation of the x-ray flux could be attributed to orbital motion of these binary systems.

2.4.1 The Wind Collision Region

The Wind Collision Region¹ is the most violent and turbulent region of a CWB system, a region where strong shocks lead to temperatures in excess of 10^8 K. These strong shocks contain enormous amounts of mechanical energy, in the region of $10^3 L_\odot$, WCRs are engines capable of producing huge quantities radiation through multiple thermal and non-thermal mechanisms (Eichler & Usov, 1993; Grimaldo et al., 2019). Despite these extreme conditions, these regions are capable of producing amorphous carbon dust grains at a rate on the order $1 \times 10^{-8} M_\odot \text{ yr}^{-1}$. As these grains are extremely fragile, this is a conundrum that has plagued researchers in this field, as direct observation of the innermost regions of even nearby WCRs is difficult, bordering on impossible, much of the work in this area involves hydrodynamical simulation.

The properties of the WCR can be described by a small number of parameters. The first of such parameters is the wind momentum ratio, η , which describes the available (Usov, 1991).

¹WCR

2. BACKGROUND

$$\eta = \frac{\dot{M}_{\text{OB}} v_{\infty}^{\text{OB}}}{\dot{M}_{\text{WR}} v_{\infty}^{\text{WR}}}, \quad (2.8)$$

This momentum ratio can also be used to estimate the distance of the apex of the WCR to each star, using the following equations:

$$r_{\text{WR}} = \frac{1}{1 + \eta^{1/2}}, \quad r_{\text{OB}} = \frac{\eta^{1/2}}{1 + \eta^{1/2}}, \quad (2.9)$$

where r_{WR} is the distance from the WR star to the WCR apex, and r_{OB} is the distance from the OB star to the WCR apex. Work by Eichler and Usov, 1993 goes further to utilise the momentum ratio to approximate the shape of the wind collision region, further out from the apex of the WCR, the region forms an approximately conical shape with an opening angle, θ_c of:

$$\theta_c \simeq 2.1 \left(1 - \frac{\eta^{2/5}}{4}\right) \eta^{-1/3}, \quad \text{for } 10^{-4} \leq \eta \leq 1, \quad (2.10)$$

2.4.2 Cooling in the WCR

Temperature range	Dominant process	Spectral region
$5 \times 10^3 \text{ K} \lesssim T \lesssim 1 \times 10^5 \text{ K}$	Forbidden lines	IR, Optical
$T \approx 1 \times 10^5 \text{ K}$	H excitation/ionisation	Optical, UV
$5 \times 10^3 \text{ K} \lesssim T \lesssim 1 \times 10^5 \text{ K}$	Resonance lines	Far UV, soft X-ray
$T \gtrsim 1 \times 10^8 \text{ K}$	Bremsstrahlung	Radio

Table 2.2: Breakdown of dominant cooling processes at various temperature ranges from Dyson, 2021, whilst H excitation/ionisation occurs over a very short temperature range, it is extremely influential, causing a global peak in the cooling rate at $\approx 10^5$ K. These temperature ranges are depicted in figure 2.4.

Cooling due to radiation emission in a hot plasma can be broken down into a variety of processes that occur over series of temperature ranges. Ions inside a plasma can become excited through collisions or photon absorption resulting in emission of photons as the ions de-excited.

Mechanisms that are significant within the warm¹ and hot gas phases include forbidden line emission, hydrogen excitation and ionisation, resonance lines and bremsstrahlung, the influence

¹See what I mean about the phrase “warm”?

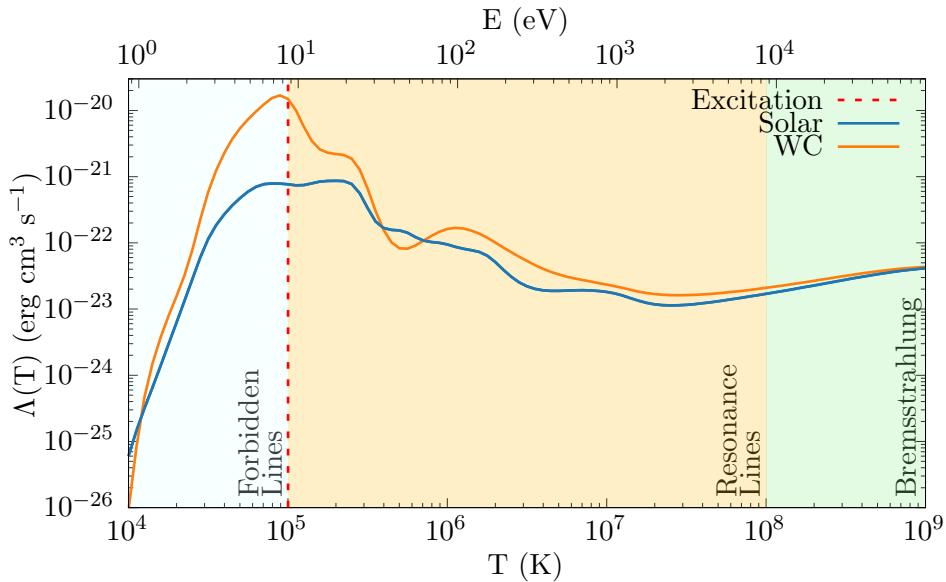


Figure 2.4: Normalised plasma cooling rates as a function of temperature and thermal energy for solar abundance and WC abundance winds. The regions where forbidden line, resonance line and bremsstrahlung emission are dominant are highlighted, with H ionisation and recombination occurring between the forbidden and resonance line sections at 10^5 K.

of each mechanism waxes and wanes as temperature increases, with each mechanism clearly dominant over (Dyson, 2021).

The first mechanism to be discussed is forbidden line emission¹. This process dominates the cooling process of cooler gas that is not fully ionised, where collisions with free electrons excite metals within the gas, causing them to de-excite through photon emission through these forbidden lines. Forbidden lines themselves arise from magnetic dipole and quadrupole fine structure states within typical energy levels, despite having a much lower probability of occurring compared to conventional energy level transitions. This process dominates at these temperatures as the transition energies are significantly lower, on the order of 1 eV, as the photon is also of a comparatively long wavelength, it can more easily escape from the gas without being re-absorbed by it.

As the temperature increases there is a spike in the cooling rate of the gas as the hydrogen

¹Like many other phenomena discussed in this thesis, this too is a misnomer, while initially assumed to be prohibited under the contemporary understanding of atomic physics, it is in fact just astrophysicists jumping the gun again.

2. BACKGROUND

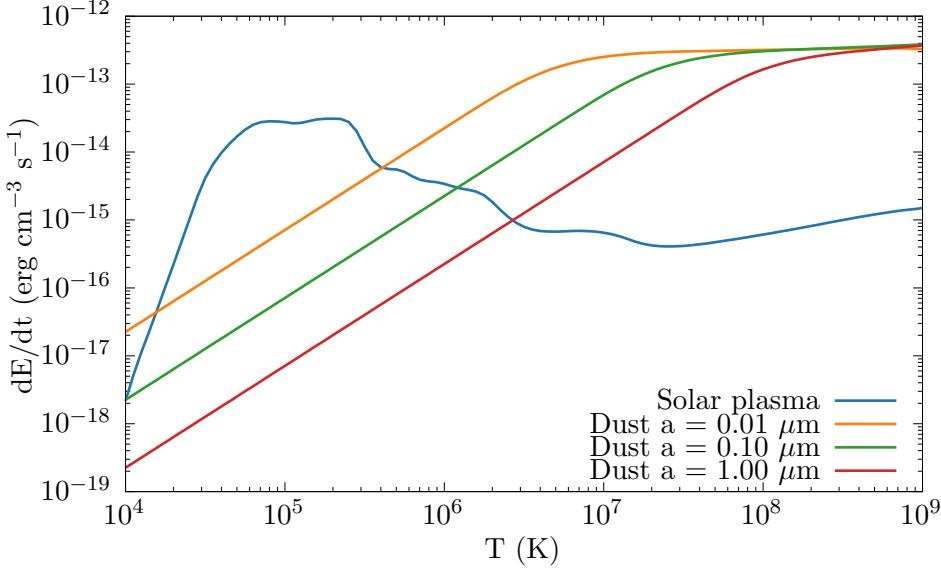


Figure 2.5: Comparison of plasma cooling to dust cooling with different grain sizes in a solar abundance gas, where $\rho_g = 10^{-20} \text{ g cm}^{-3}$ and a dust-to-gas mass ratio of 0.01.

present begins to fully ionise, at this temperature a hydrogen ion and an electron may recombine, releasing a cascade of photons as the electron de-excites.

As the plasma heats further resonance lines can

As the particle energy reaches the range of tens of keV, bremsstrahlung¹ becomes dominant (figure 2.4). High velocity electrons are deflected by ions, emitting radiation in the process due to conservation of energy.

(Schure et al., 2009) (Rybicki & Lightman, 2004)

$$\tau_{\text{cool}} = \frac{k_B T_s}{4n_w \Lambda(T_s)}, \quad (2.11a)$$

$$\tau_{\text{esc}} = \frac{d_{\text{sep}}}{c_s}, \quad (2.11b)$$

$$\chi = \frac{\tau_{\text{cool}}}{\tau_{\text{esc}}} \approx \frac{v_{\infty,8}^4 d_{\text{sep},12}}{\dot{M}_{-7}}, \quad (2.12)$$

The presence of dust within the immediate post-shock environment significantly increases the cooling rate. Figure 2.5 compares rate of cooling due to dust emission of various types of

¹Or braking radiation when you can't remember how to spell it.

grains to plasma cooling at solar abundances, As Λ_g and Λ_D are both proportional to ρ_g^2 , dust cooling will dominate at high temperatures so long as there is sufficient amounts of dust.

As dust grains collide with ionised gas and electrons, this imparts kinetic energy into the grains, heating them and causing them to emit infrared radiation. Assuming that there is a net accretion of ions and electrons onto the dust grains and the gas is optically thin in the infrared regime, energy is efficiently removed from the gas. At particularly high temperatures this effect can dominate over high-temperature plasma cooling processes such as bremsstrahlung, as seen in figure 2.5. Figure 2.6 compares dust grain heating rates due to electron and ion collisional excitation in a solar abundance and WC abundance flow. At lower temperatures the dust grain cooling rate is dominated by electron excitation, especially in the WC case as the ratio of free electrons to ions is significantly higher, as the WC flow is enriched by heavier elements. However, as the grain temperature increases, collisional heating due to ions becomes more prevalent as the electrons are sufficiently energetic to pass through the grain without significant energy transfer; this is referred to as the electron transparency, h_e (Dwek & Werner, 1981).

Work by Dwek and Werner, 1981 is used predominantly in this project to simulate cooling due to dust, a fast method for calculating the cooling rate due to dust was integrated into the numerical code for this project, which is elaborated on in section 3.9.2.

The heating rate of a dust grain due to collisions

$$H_{\text{coll}} = n\pi a^2 \langle Q(E, q, U) \rangle \times \langle v(E - qU) f(a, E - qU) f(a, E - qU) \rangle \text{ erg s}^{-1} \quad (2.13)$$

This can be simplified and expressed in the equation:

$$\begin{aligned} H_{\text{coll}} &= \left(\frac{32}{\pi m} \right)^{1/2} n\pi a^2 (k_B T)^{3/2} h(a, T) \\ &= 1.26 \times 10^{-19} \frac{n}{A^{1/2}} a^2 (\mu\text{m}) T^{3/2} h(a, T) \text{ erg s}^{-1} \end{aligned} \quad (2.14)$$

2.4.3 Dust formation in CWB systems

2.4.4 Important WCd systems

2.4.5 Contemporary research in extragalactic low-metallicity WCd systems

2. BACKGROUND

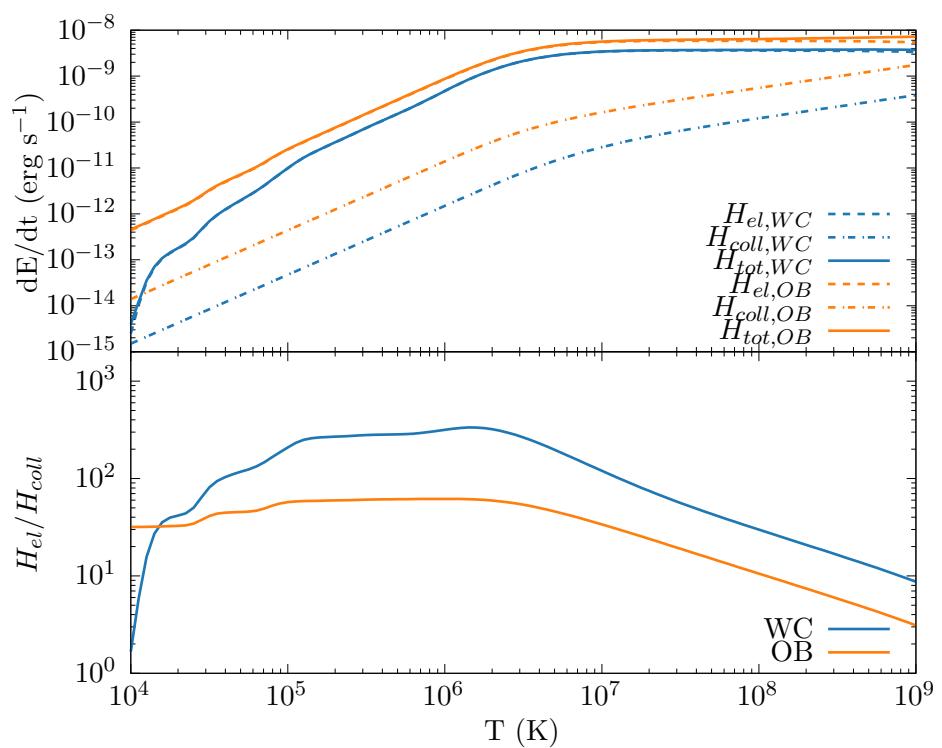


Figure 2.6: Comparison of grain heating rate due to ion collisional excitation, H_{coll} , and electron excitation, H_{el} . The dust grain has a grain radius of $5 \times 10^{-3} \mu\text{m}$ and is travelling through a gas with a density of $10^{-20} \text{ g cm}^{-3}$ with solar and WC abundances.

CHAPTER 3

Methodology & Numerical Simulation

3. METHODOLOGY & NUMERICAL SIMULATION

3.1 A Short History of Numerical simulations

3.2 The Purpose of Numerical Simulations

Numerical simulations, due to

3.3 The Mathematics of Numerical Simulations

3.4 Computational Hydrodynamics

3.4.1 Comparison of hydrodynamical methods

3.5 The Athena++ Hydrodynamical code

This is covered in more detail in the next section (section 3.6).

Athena++ is highly parallel and utilises the OpenMP and OpenMPI software libraries in order¹ Meshblocks are distributed to processor cores In the case of a simulation that requires more cores than a single computer can provide, OpenMPI is used to distribute meshblocks between nodes in a HPC² cluster, whilst this can introduce bottlenecks due to the comparatively slow networking between nodes, this allows for thousands of cores to be used, rather than dozens.

In order to prevent numerical errors from occurring between the interfaces between meshblocks, “ghost cells”, cells from adjacent meshblocks copied into the current meshblock, are used.

3.6 Mesh Refinement

One of the problems previously discussed with modelling CWB systems is the

The pseudocode for the refinement condition

```
1 // Get cell width
2 Real dx = pmb->pcoord->dx1v(0);
3 // March through cells in block, checking distance from star to cell
4 for (int n = 0; n < NWIND; n++) {
5     for (int k = pmb->ks; k <= pmb->ke; k++) {
```

¹Sadly, the engineers at Intel who worked on the Netburst architecture were [wrong](#), processors can't easily scale up to dozens of GHz, instead, multiple cores have to be used, making high performance code that much harder to write.

²High Performance Compute

3.6 Mesh Refinement

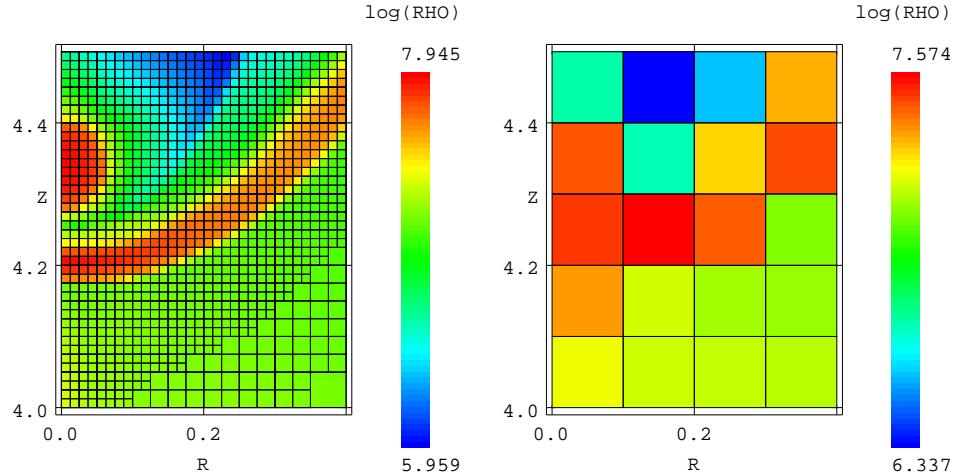


Figure 3.1: An example of adaptive mesh refinement in the MG hydrodynamical code around the OB star in a colliding wind binary problem using cylindrically symmetric coordinates. With AMR the region is properly resolved, while without the system cannot adequately resolve the collision region.

```

6   // Get Z co-ordinate separation from star
7   Real zc  = pmb->pcoord->x3v(k) - star[n].pos[2];
8   Real zc2 = SQR(zc);
9   for (int j = pmb->js; j <= pmb->je; j++) {
10    // Get Y co-ordinate separation from star
11    Real yc  = pmb->pcoord->x2v(j) - star[n].pos[1];
12    Real yc2 = SQR(yc);
13    for (int i = pmb->is; i <= pmb->ie; i++) {
14      // Get X co-ordinate separation from star
15      Real xc  = pmb->pcoord->x1v(i) - star[n].pos[0];
16      Real xc2 = SQR(xc);
17      // Get radial distance from current star to cell
18      Real r2 = xc2 + yc2 + zc2;
19      Real r  = sqrt(r2);
20      // Get approximate number of cells distance
21      int ri = int(r/dx);
22      // If number of cells distance is below threshold, refine
23      if (ri < amr.star_separation) {
24        return 1;
25      }
26    }

```

3. METHODOLOGY & NUMERICAL SIMULATION

```
27     }
28 }
29 }

1 // Check to see if meshblock contains the stagnation point
2 for (int k = pmb->ks; k <= pmb->ke; k++) {
3     // Get Z co-ordinate separation from stagnation point
4     Real zc = pmb->pcoord->x3v(k) - wcr.pos[2];
5     Real zc2 = SQR(zc);
6     for (int j = pmb->js; j <= pmb->je; j++) {
7         // Get Y co-ordinate separation from stagnation point
8         Real yc = pmb->pcoord->x2v(j) - wcr.pos[1];
9         Real yc2 = SQR(yc);
10        for (int i = pmb->is; i <= pmb->ie; i++) {
11            // Get X co-ordinate separation from stagnation point
12            Real xc = pmb->pcoord->x1v(i) - wcr.pos[0];
13            Real xc2 = SQR(xc);
14            // Get radial distance to current cell
15            Real r2 = xc2 + yc2 + zc2;
16            Real r = sqrt(r2);
17            // Get approximate number of cells between cell and stagnation point
18            int ri = int(r/dx);
19            // If number of cells distance is below threshold, refine
20            if (ri < amr.wcr_separation) {
21                return 1;
22            }
23        }
24    }
25 }
```

All cells that do not meet these criteria are flagged for de-refinement.

3.7 Visualisation

Data was plotted using a series of custom programmes designed to parse data as quickly as possible, the Python plotting library provided in the Athena++ repository was modified to incorporate Delaunay triangulation, instead of interpolating data due to mesh refinement, data-points are triangulated with each other. For 3D visualisation the VisIt data visualisation tool is used.

3.8 Simulating CWB systems

3.8.1 Assumptions

3.9 Cooling in numerical simulations

As discussed in section 2.4.2, there are many cooling processes that need to be considered when simulating a complex system such as a CWB.

Cooling is crucial to our in a purely adiabatic case, gas temperature in the post-shock region can

Additionally, adiabatic flows behave differently without a method of losing energy, density, pressure and post-shock velocity are constrained, which can drastically effect the evolution of the system, and prevent significant cooling down to the In the case of strong, adiabatic shocks, the downstream gas parameters of the system are:

$$u_b = \frac{1}{4}u_a, \quad (3.1a)$$

$$\rho_b = 4\rho_a, \quad (3.1b)$$

$$P_b = \frac{3}{4}\rho_a u_a^2, \quad (3.1c)$$

where a is the upstream side and b is the downstream, post-shock side.

in a radiative shock behaving isothermally (where the temperature change, ΔT throughout the entire lifespan of the fluid is equal to zero), the final density, ρ_f can be approximated to:

$$\rho_f \approx \gamma M_a^2 \rho_a, \quad (3.2)$$

where M_a is the pre-shock mach number. For a shock with an initial sound speed of $M_a = 100$ the final density can exceed the pre-shock density by a factor of 10^4 !

Performing radiative cooling within a numerical simulation is computationally difficult, and trade-offs between accuracy and performance must be considered at every step of designing the simulation, as every single cell must undergo cooling. For this project, the final cooling can be out by a few percent at worst, but is fast enough to run the simulations in a reasonable amount of time without excessive memory requirements. In order to simplify the radiation calculations, radiation does not re-interact with the simulation, instead it is completely removed from the simulation. Due to this, scattering, re-adsorption and radiative transfer are not simulated at

3. METHODOLOGY & NUMERICAL SIMULATION

all.¹. Other methods of reducing computational cost and optimising the code are used in this project, and will be described in detail in this section.

3.9.1 Plasma cooling

Thus, instead of calculating the emissivity of the plasma for the current density, temperature and abundance,

Exact cooling method

An exact integration scheme for radiative cooling described in Townsend, 2009 was considered to simulate cooling in Athena++.

This scheme is one of the rare example of a numerical method that is both accurate *and* fast, taking approximately the same time as a second order explicit method, whilst also being perfectly accurate even in highly radiative hypersonic flows. Unfortunately this method has a number of limitations that precluded its usage in this project. First, this method would not have been able to accurately model mixed wind situations, hampering its usage cooling winds with drastically different abundances. Second, and perhaps most importantly, only plasma cooling would have been possible, dust cooling could not be modelled at the same time, resulting in two separate cooling stages, as both mechanisms are highly temperature dependent, this was not acceptable.

3.9.2 Dust cooling

A particular difficulty in precisely calculating the rate of cooling due to emission from dust is calculating the electron transparency, h_e .² h_e can be computed via integration by parts, however due to this occurring in the main cooling loop, this results in a nesting of integrals, which can lead to extremely time-consuming computation for individual cells. The integral could be simplified by reducing the number of bins to integrate with, however below approximately 400 bins the results can become extremely inaccurate, resulting in *negative* values for h_e ; experimentation with the Initial tests using the integral method within a numerical simulation led to severe slowdown as processing time for cooling took up to 90% of the overall processing time for each timestep.

¹If these are considered, your programme is now a ray-tracing programme as well as a hydrodynamical code, which is its own, even more complicated field.

²The probability that an electron will embed in the dust grain and heat it, rather than pass through.

3.9 Cooling in numerical simulations

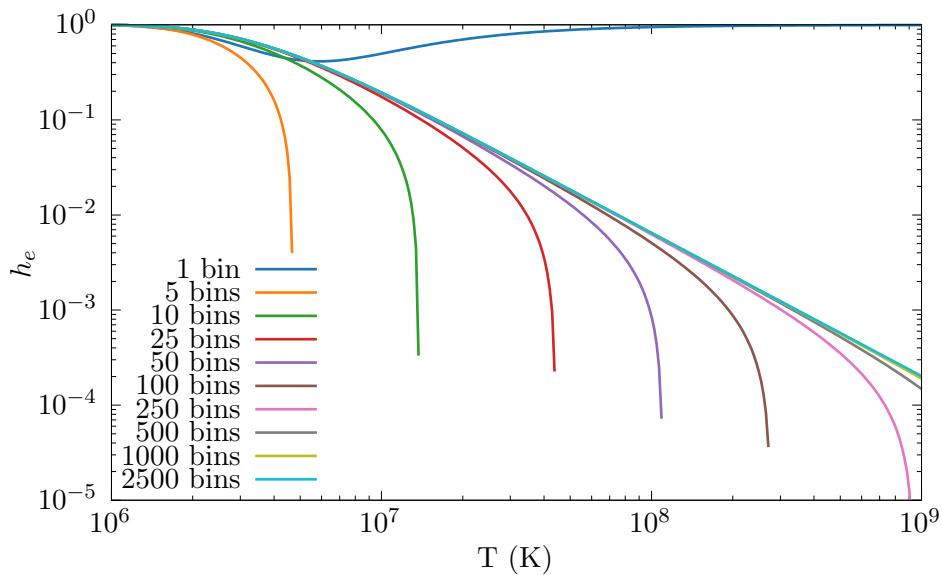


Figure 3.2: Comparison of h_e as a function of temperature for dust grains with a radius of 0.005 μm , h_e is calculated via the trapezium rule with a varying number of bins, bin counts below 500 bins result in wildly inaccurate or in some case negative values for h_e , while beyond 500 bins the result is inaccurate.

3. METHODOLOGY & NUMERICAL SIMULATION

Multiple options were considered for improving the performance of this routine. Initially, a Λ_d lookup table was considered, this consisted of a logarithmically spaced table of ρ , a , T and Λ_d values calculated by an implementation of the Dwek and Werner, 1981 prescription. A binary search for each parameter is performed, with the an offset, P_d , being calculated for each parameter,

$$P_d = \frac{P - P_0}{P_1 - P_0}, \quad (3.3)$$

these offsets are then used to perform a trilinear interpolation to calculate λ_d from the lookup table.

$$\begin{aligned} \Lambda_{00} &= \Lambda_{000} (1 - \rho_d) + \Lambda_{100} \rho_d, \\ \Lambda_{01} &= \Lambda_{001} (1 - \rho_d) + \Lambda_{101} \rho_d, \\ \Lambda_{10} &= \Lambda_{010} (1 - \rho_d) + \Lambda_{110} \rho_d, \\ \Lambda_{11} &= \Lambda_{011} (1 - \rho_d) + \Lambda_{111} \rho_d, \\ \Lambda_0 &= \Lambda_{00} (1 - a_d) + \Lambda_{10} a_d, \\ \Lambda_1 &= \Lambda_{01} (1 - a_d) + \Lambda_{11} a_d, \\ \Lambda &= \Lambda_0 (1 - T_d) + \Lambda_1 T, \end{aligned} \quad (3.4)$$

where 0 is the lookup table value lower than the parameters actual value, and 1 is the lookup table value greater than the parameters actual value. This implementation was written in the form of a series of nested loops to utilise SIMD vectorisation to improve performance.

Whilst this method is significantly faster than calculating Λ for each cell with an integration step, a $(100 \times 100 \times 100)$ lookup table requires approximately 32 MB of memory to store, and is much more time consuming to search through. As such, eliminating complexity from the binary search and reducing the number of interpolations were identified as improvements to the These optimisations were made by simplifying the lookup table into a series of smaller lookup tables and relying on even logarithmic spacing of the lookup table to determine the parameter indices, rather than performing a binary search for them. Additionally, as ρ and a are invariant within the cooling loop, these parameter offsets are solved separately using a bilinear interpolation, while in the cooling sub-step loop, a separate linear offset is performed to find the temperature offset, solving to find Λ_d . These optimisations resulted in this method scaling significantly better, as there is a lower total number of calculations required as the number of sub-steps increases (figure 3.3).

3.9 Cooling in numerical simulations

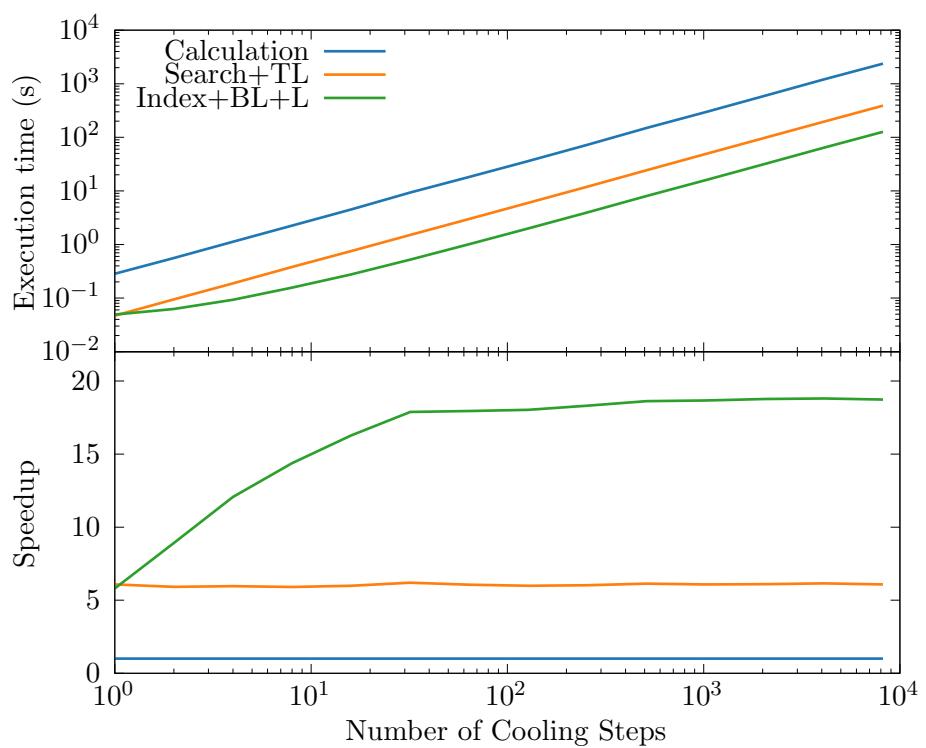


Figure 3.3: Comparison of execution time and speedup for lookup table methods.

3. METHODOLOGY & NUMERICAL SIMULATION

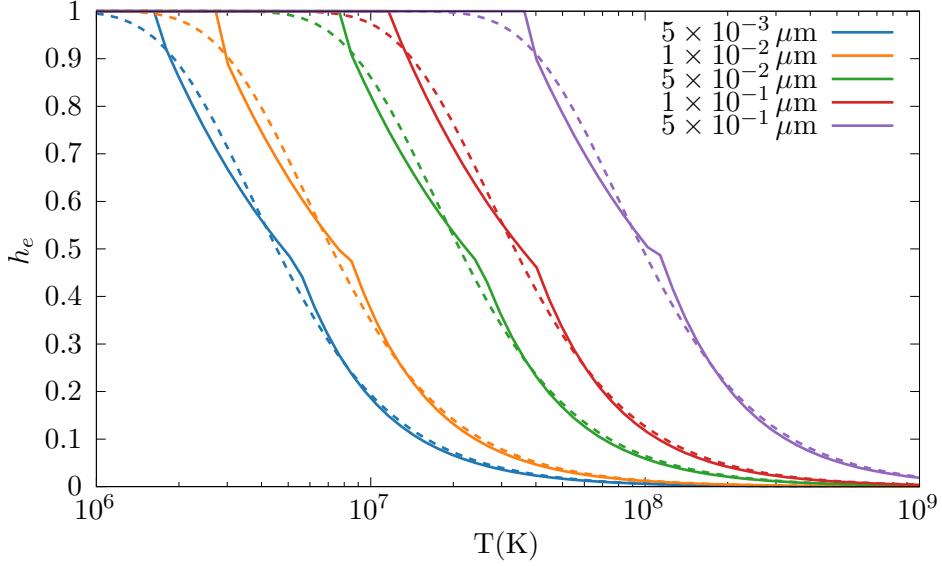


Figure 3.4: Grain transparency as a function of temperature for the estimate method described in equation 3.5 (solid lines) and a 400 bin integration method (dashed lines).

The second method considered for solving the h_e integral was using an approximation described by Dwek and Werner, 1981 where h_e could be described by a series of equations:

$$\begin{aligned} h_e(x^*) &= 1, & x^* > 4.5, \\ &= 0.37x^{*0.62}, & x^* > 1.5, \\ &= 0.27x^{*1.50}, & \text{otherwise,} \end{aligned} \quad (3.5)$$

where $x^* = 2.71 \times 10^8 a^{2/3}(\mu\text{m})/T$. Whilst this is less accurate, especially in the region where one case ends and the other begins where the result begins to diverge, this method is multiple orders of magnitude faster. Figure 3.4 shows these discrepancies, in the case where electron transparency begins to decrease the approximation is out somewhat significantly, as well as mid-way through the curve, whilst at temperatures below 10^6 K the approximation and integral methods are perfectly aligned. As the grains grow hotter and the electron transparency reduces, the influence on the cooling rate due to incident electrons reduces quite drastically, meaning that extremely high accuracy is less important at these temperatures (figure 3.5). The accuracy of the approximation method is also shown in figure 3.6, the estimated value for Λ_d closely matches the integrated value aside from the smallest dust grains at very high temperatures $T > 6 \times 10^8$ K.

Table 3.1 shows the improvements to performance inherent in the estimation method; the

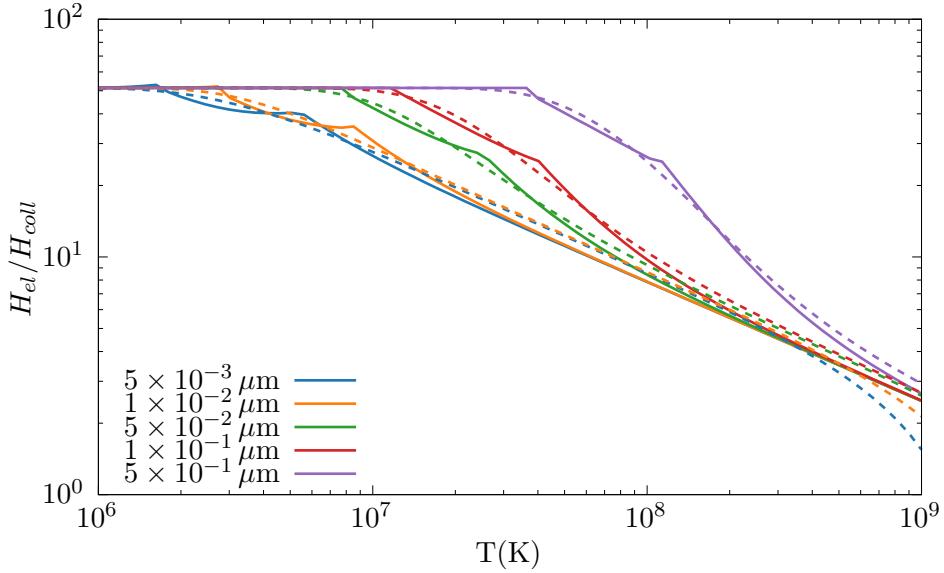


Figure 3.5: Comparison of the ratio heating rate of a dust grain due to incident electrons and incident atoms as a function of temperature for various grain sizes, whilst the result between the integration method and estimate method diverge, this is while the contribution of heating from electrons becomes less influential on the cooling rate of the grain.

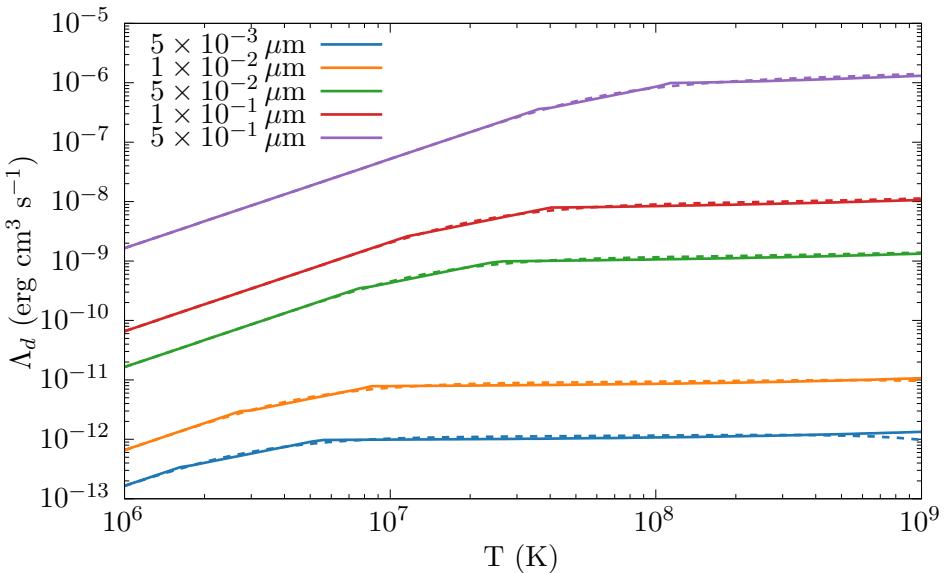


Figure 3.6: Λ_d as a function of temperature for various grain sizes, the estimate method is extremely close to the integral value aside from at the highest temperatures.

3. METHODOLOGY & NUMERICAL SIMULATION

Method	t(s)	Iter/s	Speedup
400 bin integration by parts	36.03	35,526	-
Binary search + trilinear	6.016	212,751	599%
Index calculation + bilinear + linear	1.999	640,447	1,803%
Dwek and Werner, 1981 approximation	0.147	8,693,171	24,510%

Table 3.1: Comparison of methods explored for estimating $\Lambda_d(\rho, a, T)$ in cooling code, 10^4 initial values were chosen and 128 cooling sub-steps were performed, benchmark code was compiled and run using GCC 10.3.0 with the -O3 optimisation set on an Intel i7-7700HQ processor with a maximum clock speed of 3.8 GHz.

final result is that the approximation is over 24,500% faster, the resulting dust cooling function therefore will have a minimal computational impact on the cooling loop as a whole. As this approximation was conclusively shown to not significantly effect the cooling rate due to grain heating, the approximation was chosen.

Further improvements were made to correctly determine the electron number, n_e , to calculate the cooling contribution for dust due to grain-electron collisions. the initial version of this code assumed that $n_e = 1.1n_p$, an estimate based on solar abundances, however the electron-to-ion ratio varies significantly with temperature in a WC wind, which is hydrogen depleted and as such can vary from 0 to ~ 4 between 1×10^4 and 5×10^6 K (figure 3.7). In order to solve this problem quickly for each timestep, a lookup table similar to the plasma cooling curves was used, containing the electron-ion ratio at temperatures between 10^4 and 10^8 K for each wind abundance.

3.9.3 Implementation

In order to simulate energy loss due to radiation in Athena++, the conserved variable array is adjusted to remove energy from a specific cell, this is analogous to energy being removed from the system due to radiative processes. This process is assumed to be 100% efficient, re-adsorption and scattering is not simulated, as this would be very complex to simulate at every time step.

Radiative processes are part of a source function that is performed for every mesh block. The cooling routine within the source function iterates through all cells within the meshblock, calculating radiative energy loss for each cell. Within the loop, the cell parameters are loaded from the conserved variables array, and additional gas and dust parameters are calculated from

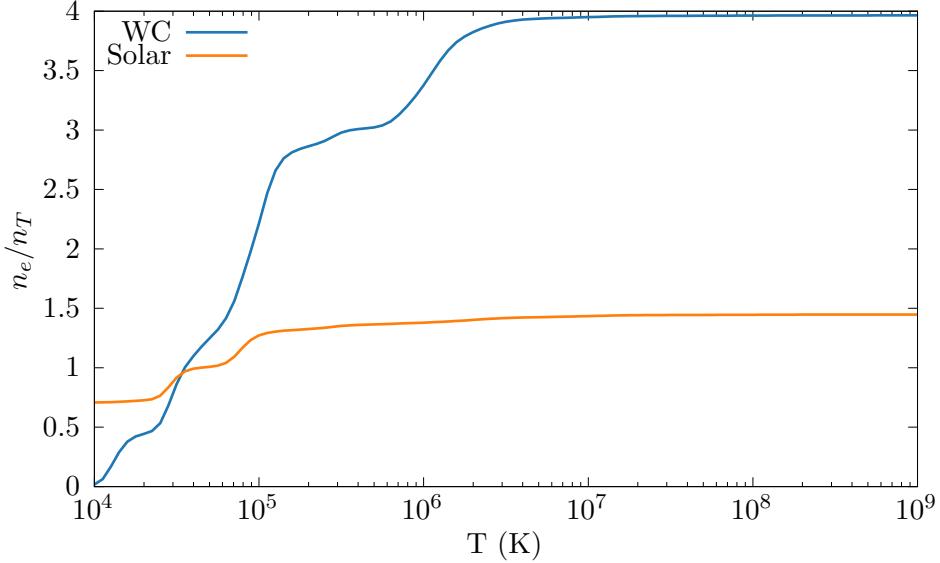


Figure 3.7: Ionisation fraction

these conserved variables. in particular the mean molecular mass of a cell is calculated with the formulae:

$$\mu = C\mu_{WR} + (1 - C)\mu_{OB}, \quad (3.6)$$

where μ_{WR} and μ_{OB} are the mean molecular masses of the winds and C is the wind “colour” scalar, the contribution of each wind to the gas density of the cell. The temperature is subsequently calculated using the ideal gas law:

$$T = \frac{P\mu m_H}{\rho k_B}. \quad (3.7)$$

At the current temperature, the cooling parameter, $\Lambda(T)$ for each wind is found from the lookup tables, and weighted in a similar manner as equation 3.6. The energy loss due to dust grains is then calculated, with the total energy loss rate within the cell defined as:

$$\dot{E} = \dot{E}_G + \dot{E}_D = \left(\frac{\rho}{m_H} \right)^2 \Lambda_G(T) + n_D \dot{E}_{\text{grain}}, \quad (3.8)$$

this energy loss rate is then multiplied by the timestep, dt , and then subtracted from the total energy within the cell.

One of the main issues with estimating the cooling rate rather than performing an exact calculation of energy loss is that the cooling rate and current temperature are coupled, this

3. METHODOLOGY & NUMERICAL SIMULATION

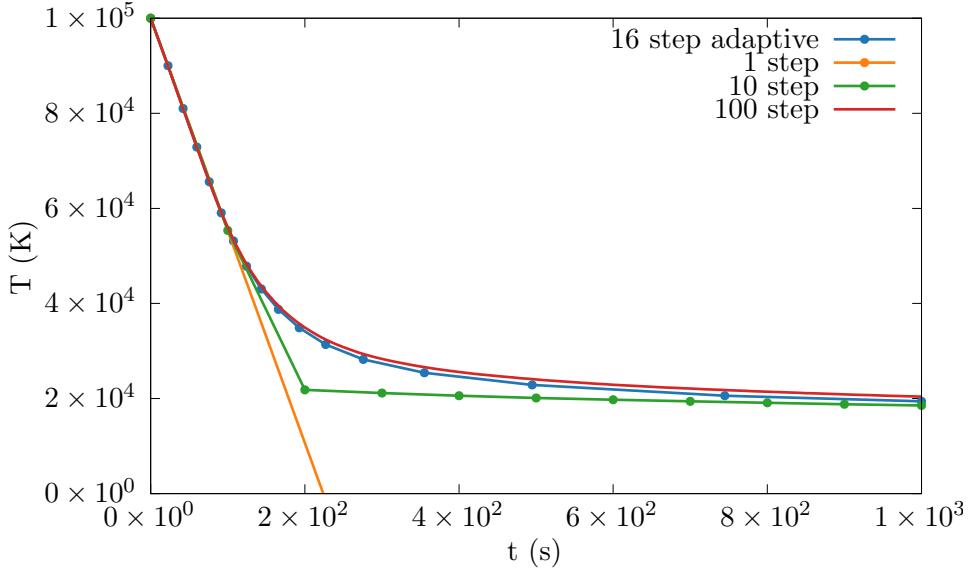


Figure 3.8: Comparison of the adaptive timestep method versus linearly spaced sub-steps for a solar abundance flow with a density of $10^{-16} \text{ g cm}^{-3}$ and an initial temperature of 10^5 K .

can result in wildly inaccurate final temperatures at the end of the cooling step compared with an exact integration. This is especially a concern at the expected temperatures in the post-shock, radiatively cooled environment, as the $\Lambda(T)$ is maximised at approximately 10^5 K . If the timestep is too large this can result in over-estimation of the cooling. The simplest solution would be to make the time-step smaller, however this would reduce the performance of the code, as the cooling loop takes significantly less time to perform than the hydrodynamical loop. Instead, adaptive sub-stepping is used to iterate through the time-step, adjusting the maximum sub-step for an integration based on the current gas parameters, specifically the amount of energy remaining in the cell. Figure 3.8 shows the adaptive sub-stepping routine in operation, at the initial time, the cooling parameter Λ is maximised, as such the time-step is significantly lower than when the gas has cooled as is less radiative. This compares favourably to a single sub-step example, which would cause the simulation to crash due to negative temperatures, and with linearly spaced steps, which either required many more steps or were potentially unstable.

A suitably accurate maximum cooling time is calculated by first calculating the cooling time in the cell using the formulae:

$$\tau_{\text{cool}} = \frac{E_i}{\dot{E}_{\text{iter}}}, \quad (3.9)$$

where E_i is the cells internal energy and \dot{E}_{iter} is the total energy loss rate for the current iteration. A fraction of this value is used as the sub-timestep, which is used to calculate the energy loss in that iteration.

$$dt_{\text{step}} = \kappa \tau_{\text{cool}}, \quad (3.10)$$

Another iteration of the cooling calculation is then performed, with sub-step time re-calculated, until the elapsed time is equal to the hydrodynamical timestep, dt . Throughout the simulations in this project a value of $\kappa = 0.1$ was adopted.

In order to assess the performance and accuracy of this method, a test environment was produced to simulate the radiation of a region of gas in the post-shock environment. For this test, a gas density of $10^{-16} \text{ g cm}^{-3}$ and an integration timestep of 1000 s were utilised. In order to demonstrate the flexibility of the adaptive method over the temperature ranges of a CWB simulation, initial temperatures of 10^5 , 10^6 and 10^7 K were used to demonstrate the models effectiveness in the cool, warm¹ and hot regimes of the WCR. This was compared with the exact integration method proposed in Townsend, 2009 as well as a modified version of the cooling code which uses evenly spaced sub-steps. To demonstrate the relative accuracy of the chosen cooling timescale fraction, lower values of κ were also used to demonstrate that lower values, while more accurate, were much more computationally complex.

The main limitation of a first-order Euler integration method such as this is that it converges on the correct answer slowly, and as such will be out by a few percent in the worst case so long as a sensible sub-step is used. Table 3.3 shows that while an iteration of the logarithmic index method used in this project is slightly more performant than the fast exact integration method proposed in Townsend, 2009, multiple sub-steps quickly render this performance benefit moot, in high-temperature cases with a lower gas density this method is much more accurate with fewer steps, however, as such this method was considered suitable for performing radiative cooling in the high-temperature immediate post-shock environment and lower density low-temperature WCR environment, where the bulk of this project focusses.

Whilst this is a fairly simplistic method of performing adaptive sub-stepping, it is fast, effective, and not prone to failure. An adaptive RK method and implicit method were also

¹See what I mean about the phrase “warm”?

3. METHODOLOGY & NUMERICAL SIMULATION

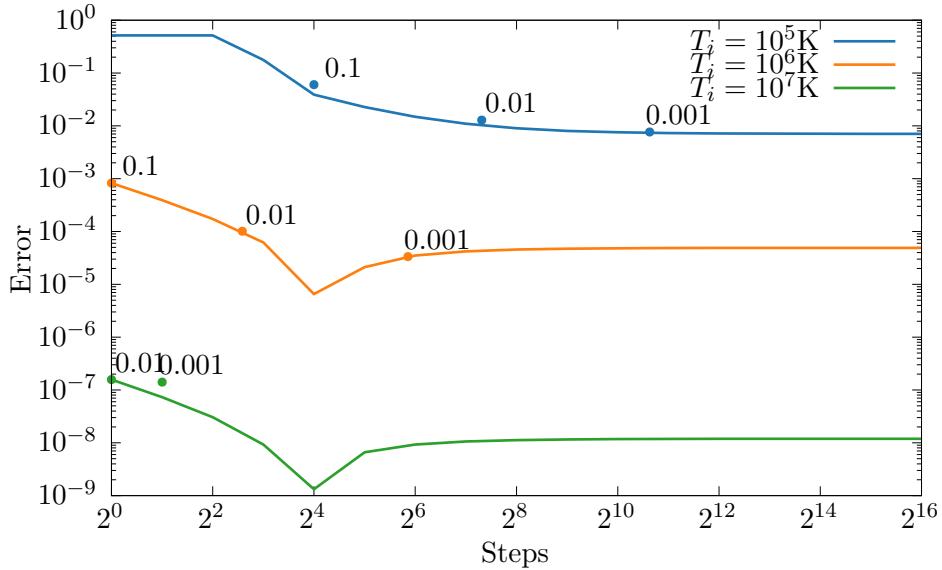


Figure 3.9: Comparison of estimated , points represent κ , in the low temperature case the answer is not particularly accurate, but with the adaptive method with $\kappa = 0.1$ the result is only out by a few percent for a small number of sub-steps.

considered, but not utilised in the final code, as this sub-stepping procedure was intended for speed and numerical safety over accuracy.

Care is made to correctly calculate energy loss around unresolved interfaces. *Finish this!*

3.10 The BODMAS Adverted Scalar Dust Model

Binary Orbit Dust Model with Accretion and Sputtering¹

The primary focus of this project was to implement a dust model within a numerical simulation, in order to determine the growth of dust grains within the

¹All good theses have a laboured acronym!

3.10 The BODMAS Advected Scalar Dust Model

	$\kappa = 0.1$		$\kappa = 0.01$		$\kappa = 0.001$	
T_i	Steps	Error	Steps	Error	Steps	Error
1×10^5 K	16	6.025×10^{-2}	159	1.282×10^{-2}	1585	7.637×10^{-3}
1×10^6 K	1	8.233×10^{-4}	6	1.012×10^{-4}	58	3.359×10^{-5}
1×10^7 K	1	1.577×10^{-7}	1	1.577×10^{-7}	2	1.411×10^{-7}

Table 3.2: Accuracy of the adaptive sub-step Euler method compared with the Townsend, 2009 exact cooling method, with $\kappa = 0.1$ this method is out by 6% at worst in the low-temperature example, while very accurate at higher temperatures with only a single step needed.

	Search	Logarithmic	Townsend, 2009
τ (ns)	146	134	151
$\Delta\tau$ (ns)	8.0	1.5	0.9

Table 3.3: Comparison of performance between first order Euler integration methods and the exact integration method described by Townsend, 2009. Tests were conducted with a sample of 10^6 iterations on a 3.2 GHz M1 processor, while the code was compiled using `clang 12.0.5` and the `-O3` optimisation set.

3.10.1 BODMAS features

3.10.2 Contemporary dust Models

The Hendrix dust model

Perhaps the most similar contemporary dust model is the model described in Hendrix et al., 2016 - as this model is concerned with simulating the dynamics of dust within a CWB. This is not to say that these models are identical, of course, as the Hendrix model explores how dust spreads throughout the WCR of WR 98a, in order to compare with observational data using radiative transfer code.

The main differentiating factors between this model and our model are the driving mechanism and dust evolution. In the Hendrix model dust is modelled as a separate fluid, with an Epstein drag function between the wind and dust fluids; this method allows for dust kinematics that aren't implicitly co-moving. This is a more accurate method of modelling dust, however it requires significantly more processing time and is much more difficult to implement, requiring a

3. METHODOLOGY & NUMERICAL SIMULATION

numerical code that supports multiple fluids. At the start of this PhD this was considered but eventually rejected due to time constraints.

The purpose of the Hendrix model is to analyse the distribution of dust within a CWB system, rather than to model the evolution of the dust itself. To this end, the Hendrix model does not

3.10.3 Implementation

3.10.4 Future dust models

Due to time constraints and limitations in the code in use, only a limited set of mechanisms for dust evolution were included in this projects simulations. While the BODMAS model represents an interesting start for the modelling of dust grains in colliding wind binaries, future models could implement more complex models which incorporate additional destruction and growth mechanisms as well as

A multi-scalar model could be used to more accurately measure the growth of dust grains, rather than a single average grain size and This would be more difficult to implement than a single model but would be able to simulate the growth of grains with a large number Athena++ and MG both have issues with a large number of scalars, as such both numerical codes may require significant modification to cope with this. A multi-fluid model with dust being physically simulated rather than assumed to be perfectly co-moving would be an ideal next step. Multiple grain size distributions could also be modelled in a similar way to the proposed multi-scalar model, however the kinematics of the dust grains could also be simulated separately. The increased inertia of more massive dust grains could result in the kinematics of the dust flow diverging from the co-moving assumption. To that end, a successor dust model would adopt a multi-fluid and drag function method, which was considered but not included for the sake of time. This multi-fluid model would also allow for more physically accurate simulation of grain-gas and grain-grain interactions, as the collision velocities would be exactly calculated rather than estimated through bulk motion properties, high speed collision of gas on dust grains in the immediate post-shock environment could also shatter grains, though modelling this as well as spalling of particles in the wind through the dust grains would be complex to simulate.

Furthermore, additional mechanisms for dust destruction, such as through photodissociation and sublimation could also be implemented, the implementation of these could be used to determine the effectiveness of the WCR in protecting nascent, still forming dust grains.

The initial grain nucleation model could also be improved, injection of extremely small grains

3.10 The BODMAS Adverted Scalar Dust Model

into the simulation through the stellar remap zones was chosen as the underlying chemical process for formulation of these dust grains is poorly understood at the time of writing. The small grain nucleation model was also found to be only dependent on the initial grain radius, a_i , whilst changing the amount of grain nuclei in the WR wind does not change the amount of dust produced. As such the simulations are currently bound by a single input parameter, which can be constrained based on what is currently understood about dust grain accretion. A more complex model may require additional parameters, and as such would be highly dependent on them.

Another avenue of future research would be performing a radiative transfer simulation upon a fully advected system, in order to compare with This was initially considered at the start of the project, but was not performed due to the limited amount of time remaining at the end of the PhD. This was performed by Hendrix et al. (2016), with the resultant images emulating the sensitivity and angular resolution characteristics of UKIRT, Keck and ALMA (figure 3.10). Radiative transfer models would be used to

3. METHODOLOGY & NUMERICAL SIMULATION

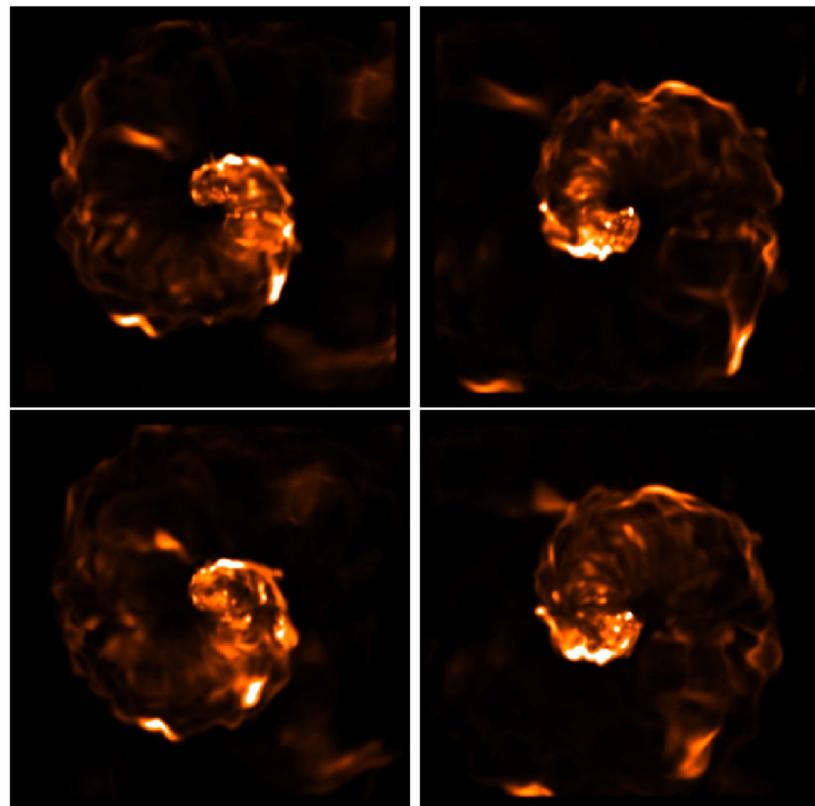


Figure 3.10: Synthetic images of WR 98a emulating the capabilities of ALMA using a radiative transfer model, reproduced from Hendrix et al. (2016).

CHAPTER 4

A Parameter Space Exploration of Dust Formation
within WCd Systems Using an Advectored Scalar Dust
Model

4. A PARAMETER SPACE EXPLORATION OF DUST FORMATION

Abstract

4.1 Introduction

Binary systems with colliding stellar winds are a fascinating phenomena capable of producing a variety of phenomena. The shocks produced from these interacting systems create some of the most luminous persistent stellar-mass X-ray sources in the night sky (Usov, 1991). Within the wind collision region the available mechanical energy rivals the radiative energy of many stars, producing shocks with temperatures up to 10^8 K.

Despite this, in particularly energetic Colliding Wind Binary (CWB) systems, such as those with an evolved Wolf-Rayet (in particular the WC sub-type) star as the source of the dominant wind in the system (A WR+OB binary), dust has been observed to form. Allen et al. (1972) first attributed IR excess around WC systems to dust in the form of amorphous carbon grains; however, the high wind temperatures and extremely high luminosities around WC systems are such that dust grains would be readily destroyed through sublimation processes. Despite this, dust has been observed to form readily in binary systems (a WCd system), despite an additional highly luminous star and shocks that would quickly destroy dust acting upon these nascent, fragile dust grains. The exact mechanisms of dust formation as well as the evolution of dust within these systems is poorly understood. However dust formation rates can be extremely high, up to $10^{-8} M_\odot \text{ yr}^{-1}$, or approximately 0.1% of the total wind by mass.

Within different colliding wind binary systems, Dust may form either continuously or periodically. Whilst the exact mechanism for this condition is not currently known, there is a strong correlation between periodicity and eccentricity, with less eccentric systems forming dust continuously, while highly elliptic systems exhibit periodic dust formation. Due to this orbital dependency, it is likely that there is an optimal dust forming separation, where dust can form in large quantities. This could be due to factors such as strong post shock cooling, which is highly dependent on the wind speed and orbital separation. Additionally, dust may be protected from the bulk of the stellar radiation due to the extremely large degree of extinction from the dense post-shock environment.

4.1 Introduction

Direct observation of dust forming CWBs and in particular the Wind Collision Region (WCR) is exceptionally difficult for a number of reasons:

- WR+OB CWB systems are extremely rare, of the 667 catalogued WR stars at time of writing, 106 have been confirmed to be in a binary system (Rosslowe & Crowther, 2015).
- A WC star is required for dust formation, no Nitrogen sub-type Wolf-Rayet (WN) have been observed to form dust. At time of writing 41 WR binaries contain WC stars.
- Not all WC+OB systems are dust producing, limiting the sample size further.
- Galactic CWB systems are comparatively distant from earth. For instance, WR 104, a well-studied system, is ~ 2.5 kpc distant. This prevents observations of these systems at a high angular resolution.
- Based on work by Zubko (1998) of CWB systems it appears that grain growth from small nucleation grains is quite rapid, this means that studying the initial grain evolution requires extremely high angular resolution observations.

For these reasons, numerical simulations are useful for modelling the growth of dust grains within this unresolved region. In order to better understand what influences dust production in a CWB system, a parameter space exploration of the wind and orbital parameters was performed. In particular the orbital separation, mass-loss rate and wind velocity were modified for both stars in order to influence the wind momentum ratio, η , and the cooling parameter, χ . The wind momentum ratio is defined as

$$\eta = \frac{\dot{M}_{\text{OB}} v_{\text{OB}}^{\infty}}{\dot{M}_{\text{WR}} v_{\text{WR}}^{\infty}}, \quad (4.1)$$

where \dot{M} is the mass loss rate of a star and v^{∞} is the terminal velocity of a star's outflow. A low value for η indicates that the winds are extremely imbalanced, with one star dominating the wind dynamics of the system. The wind momentum ratio sets for a given orbital separation, d_{sep} , the distance from each star to the apex of the wind collision

$$r_{\text{WR}} = \frac{1}{1 + \eta^{1/2}} d_{\text{sep}}, \quad (4.2a)$$

$$r_{\text{OB}} = \frac{\eta^{1/2}}{1 + \eta^{1/2}} d_{\text{sep}}. \quad (4.2b)$$

4. A PARAMETER SPACE EXPLORATION OF DUST FORMATION

In the case of a very small wind momentum ratio the primary star's wind completely envelopes the secondary stars forming an approximately conical WCR surface. The half-opening angle of this surface can be estimated by

$$\theta_c \simeq 2.1 \left(1 - \frac{\eta^{2/5}}{4} \right) \eta^{-1/3} \quad \text{for } 10^{-4} \leq \eta \leq 1, \quad (4.3)$$

to a high degree of accuracy (Eichler and Usov, 1993, but also see Pittard and Dawson, 2018). The cooling parameter, χ , compares the cooling time to the escape time from the shock region for a parcel of gas in the immediate post-shock environment. An approximation can be made using the known parameters of a system using the equation:

$$\chi = \frac{t_{\text{cool}}}{t_{\text{esc}}} \approx \frac{v_8^4 d_{12}}{\dot{M}_{-7}}, \quad (4.4)$$

where v_8 is the wind terminal velocity in units of 10^8 cm s^{-1} , d_{12} is the distance to the WCR apex in units of 10^{12} cm , and \dot{M}_{-7} is the mass loss rate in units of $10^{-7} M_\odot \text{ yr}^{-1}$ (Stevens et al., 1992). Small values of χ indicate that radiative cooling is very important, while $\chi \gg 1$ indicates an adiabatic system. Strong cooling occurs in comparatively slow, dense winds and is aided by a high metallicity. As such in many systems the post-shock WR flow will rapidly cool from the immediate post-shock temperature of 10^8 K to temperatures in the dust formation range, $\lesssim 10^4 \text{ K}$. A strongly radiating WCR can be compressed far more as it loses energy. In comparison, an adiabatic WCR is limited to a maximum density increase of a factor of 4 above the pre-shock wind density. This, combined with the reduction in gas temperature results in rapid dust growth and protection from the stellar UV radiation.

4.2 Methodology

Numerical simulations within this paper utilise the Athena++ hydrodynamical code, a highly modular modern fluid dynamics code (Stone et al., 2020). Simulations are generated in 3D and the Euler hydrodynamical equations are solved in the form:

$$\frac{\partial \rho}{\partial t} + \nabla \cdot (\rho \mathbf{u}) = 0, \quad (4.5a)$$

$$\frac{\partial \rho \mathbf{u}}{\partial t} + \nabla \cdot (\rho \mathbf{u} \mathbf{u} + P) = 0, \quad (4.5b)$$

$$\frac{\partial \rho \varepsilon}{\partial t} + \nabla \cdot [\mathbf{u} (\rho \varepsilon + P)] = \dot{E}_{\text{cool}}, \quad (4.5c)$$

4.2 Methodology

where ε is the total specific energy ($\varepsilon = \mathbf{u}^2/2 + e/\rho$, ρ) is the mass density, e is the internal energy density, P is the gas pressure and \mathbf{u} is the gas velocity. In order to simulate radiative losses, the parameter \dot{E}_{cool} is included, which is the energy loss rate per unit volume from the fluid due to gas and dust cooling, which is elaborated on in section 4.2.1.

Athena++ has been configured to run using a piecewise linear reconstruction method with a 4th order Strong Stability Preserving Runge-Kutta time-integration method (Spiteri & Ruuth, 2002). Athena++ was forked from the original repository and additional routines were written for a Colliding Wind Binary case. Routines were created to produce a steady outflow from a small spherical region around a set of cartesian co-ordinates as well as a function to move these co-ordinates with each time-step; these were used to simulate stellar wind outflow and orbital motion, respectively. Additionally, Athena++ was further modified to include an advected scalar dust model for simulating dust growth and destruction as well as a photon emission cooling model to approximate cooling for gas and dust particles within the fluid.

Athena++ utilises OpenMPI for parallelism, breaking the simulation into blocks, which are distributed between processors. The block size is variable, but for these simulations a block size of $32 \times 32 \times 8$ was found to be optimal. This meshblock system is also utilised in mesh refinement for increasing effective resolution. As the CWB systems are being simulated in their entirety, a very large volume needs to be simulated, while at the same time the region between the stars must be resolved with a resolution of at least 100 cells in order to adequately resolve the WCR. This difference in length scales necessitates the use of static mesh refinement (SMR) to improve the effective resolution of the simulation. A base coarse resolution of $320 \times 320 \times 40$ cells is defined for the simulations, while a region close to the binary pair operates at a higher refinement level, resulting in a resolution increase with a factor of 2^{n-1} greater than the coarse resolution, where n is the refinement level (figure 4.1). This results in an effective resolution of $20480 \times 20480 \times 2560$ cells. SMR is utilised instead of Adaptive Mesh Refinement, a more flexible conditional method, as it has proven to be more reliable within Athena++, as it mitigates unintentional over-refinement. As much of the grain evolution occurs a small distance from the WCR stagnation point, much of the simulation can be run at a lower resolution without affecting the simulation outcome.

The wind outflow from each star is simulated by replacing the conserved variables (density, momentum and energy) within a small region around the expected position of the stars; this region is typically on the order of 6 maximally refined cells in radius. This rewrite corresponds to a change in mass and mechanical energy imparted by an outflowing wind, such that

4. A PARAMETER SPACE EXPLORATION OF DUST FORMATION

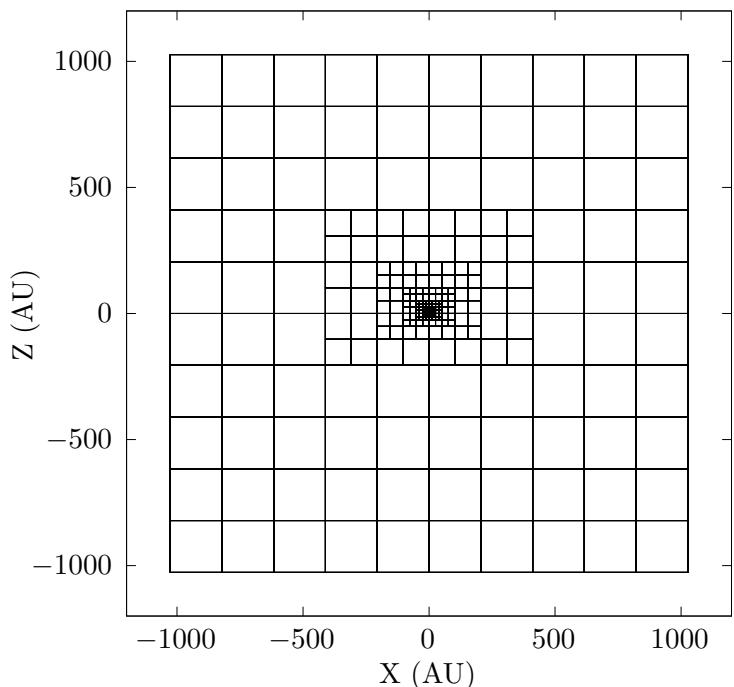


Figure 4.1: Plot of blocks used in a 7 level simulation with a block size of $32 \times 32 \times 8$ cells. The block density increases dramatically closer to the barycentre.

$$\rho_R = \frac{\dot{M}}{(4\pi r^2 v_\infty)}, \quad (4.6a)$$

$$p_R = \rho_R v_\infty, \quad (4.6b)$$

$$E_R = \frac{P_R}{\gamma - 1} + \frac{1}{2} \rho_R v_\infty^2, \quad (4.6c)$$

where v_r is the wind velocity as it flows radially from the center of the “remap zone”, P_R is the remap pressure, $P_R = \rho_R k_B T_w / \mu m_H$, T_w is the wind temperature and r is the distance from the current cell to the centre of the remap zone. Orbits are calculated by moving the remap zones in a manner consistent with Keplerian dynamics, which are updated at every timestep.

4.2.1 Gas and dust cooling

Cooling due to photon emission from atoms, ions and free electrons, as well as dust particles is simulated by removing energy from a cell at each timestep. The total energy loss is calculated by integrating the energy loss rates due to gas, plasma and dust cooling using the Euler method; in regions with very rapid cooling sub-stepping is used to improve accuracy, with the number of sub-steps being determined by comparing the substep time to the cooling timescale of the cell. Gas cooling is simulated using a lookup table method. A data file containing the gas temperature and associated normalised emissivity, $\Lambda(T)$ of the wind at that temperature is read into the simulation. In a typical cooling step, the temperature is calculated and a binary search is performed to find the nearest temperature in the lookup table. A linear interpolation is then performed to find an appropriate value for Λ . Energy loss can be calculated with the formulae:

$$\frac{dE}{dt} = \left(\frac{\rho}{m_H} \right)^2 \Lambda_w(T), \quad (4.7)$$

where ρ is the gas density and m_H is the mass of a hydrogen atom. The lookup table was generated by mixing a series of cooling curves generated by MEKAL simulations of elemental gasses. These are combined based on the elemental abundances of each wind such that:

$$\Lambda_{\text{WR}}(T) = n_e n_i \sum X_{\text{WR}} \Lambda_{\text{WR}} E(T), \quad (4.8a)$$

$$\Lambda_{\text{OB}}(T) = n_e n_i \sum X_{\text{OB}} \Lambda_{\text{OB}} E(T), \quad (4.8b)$$

where n_e and n_i are the electron and ion number density, X is the abundance of an element, and $\Lambda_E(T)$ is the cooling parameter of an element. Figure 4.2 shows the cooling curves used for

4. A PARAMETER SPACE EXPLORATION OF DUST FORMATION

	X(E)	
	Solar	WC9
H	0.705	0.0
He	0.275	0.546
C	3.07×10^{-3}	0.4
N	1.11×10^{-3}	0.0
O	9.60×10^{-3}	0.05

Table 4.1: Abundances used for the OB and WR stars being simulated, other elements are assumed trace when calculating radiative energy loss due to dust.

each star. Two lookup tables are used in the simulations, based on the elemental abundances of each star. The Wolf-Rayet star uses a curve with abundances typical of a WC9 star with total hydrogen depletion and a high carbon mass fraction, while the OB star is assumed to have solar abundances. The most significant abundances used in this projects simulations are presented in table 4.1. The cooling regime of this code ranges from 10^4 to 10^9 K. A floor temperature of 10^4 K is implemented, temperatures between 1×10^4 K $< T \leq 1.1 \times 10^4$ K are reduced to 10^4 K as they are assumed to be either rapidly cooling or a part of the stellar wind.

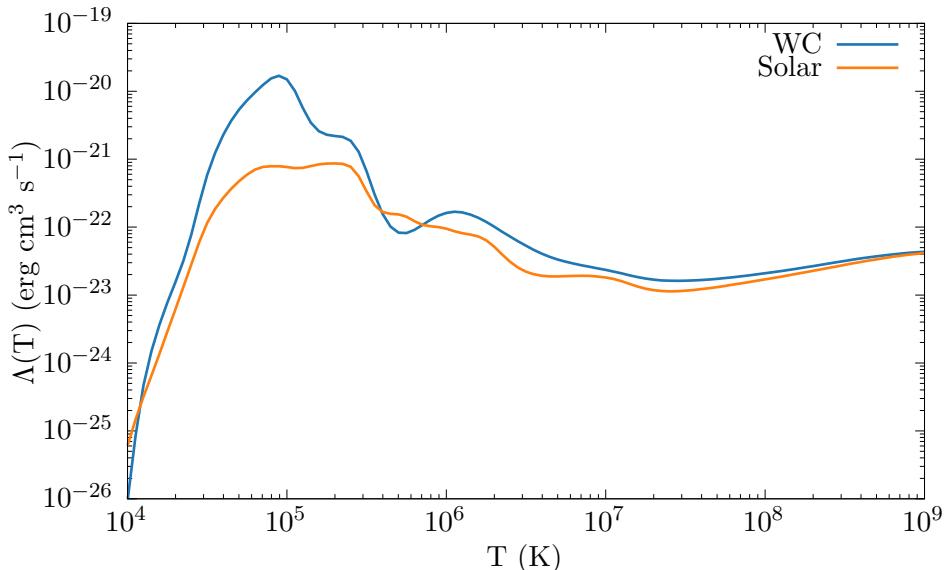


Figure 4.2: Comparison of lookup tables for calculating energy loss due to gas cooling.

4.2 Methodology

A model for cooling due to emission from dust grains is also included as dust cooling is expected to play a significant role in the evolution of each system. The rate of cooling is calculated using the uncharged particle case of the Dwek and Werner (1981) prescription. Grains are heated due to collisions with ions and electrons, causing them to radiate, with energy being removed from the simulation. This assumes that the region being simulated is optically thin to far infrared photons. The energy loss rate is calculated with the following formulae:

$$H_{\text{coll}} = 1.26 \times 10^{-19} \frac{n}{A^{1/2}} a^2 (\mu\text{m}) T^{3/2} h(a, T), \quad (4.9a)$$

$$\Lambda_d = \frac{H_{\text{coll}} + H_{\text{el}}}{n_H}, \quad (4.9b)$$

$$\frac{dE}{dt} = n_T n_d \Lambda_d, \quad (4.9c)$$

where H_{coll} is the heating rate due to atom and ion collisions, H_{el} is the heating rate due to electron collisions, $h(a, T)$ is the grain-ion transparency and n_T is the total ion number density. H_{coll} is summated for Hydrogen, Helium, Carbon, Nitrogen and Oxygen atom collisions. Other elements are not considered as they are present in trivial proportions in both winds.

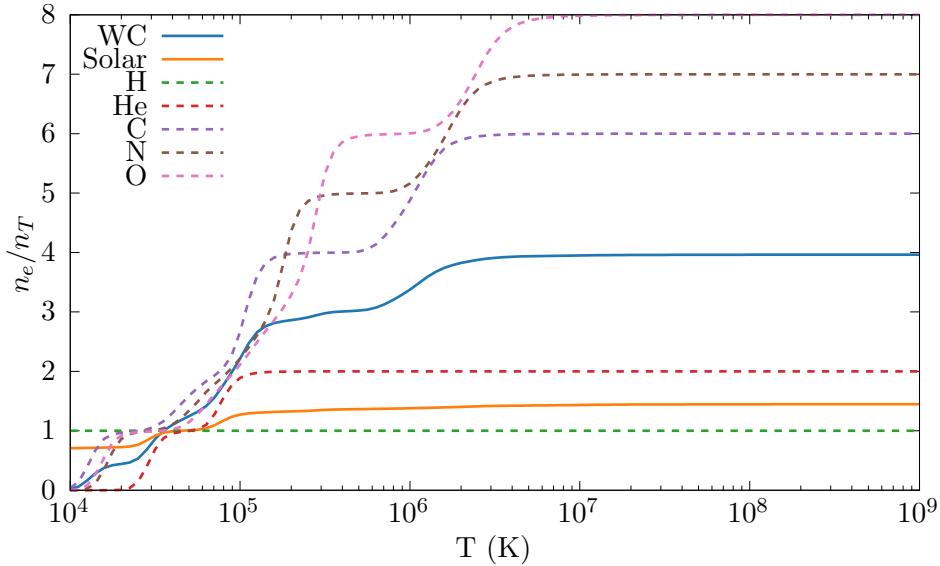


Figure 4.3: A comparison of the electron-ion ratio of both winds as the temperature changes. Included are the pure wind flows that the lookup tables are built from.

Electron-grain collisions are modelled similarly to ions, albeit with some differences. One major factor for calculating accurate energy loss due to electron collisions is that the electron

4. A PARAMETER SPACE EXPLORATION OF DUST FORMATION

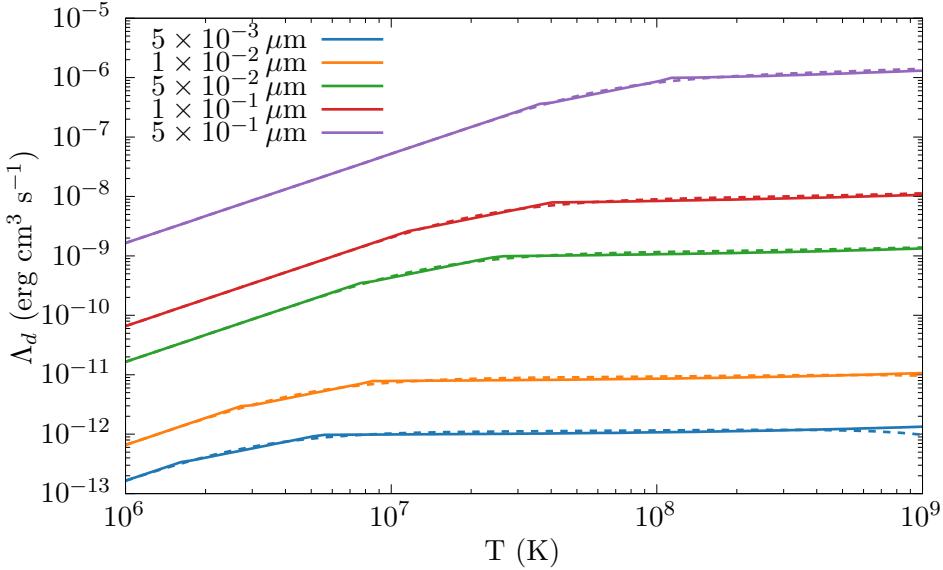


Figure 4.4: Λ_d as a function of temperature for various grain sizes. The estimate method is extremely close to the integral value aside from at the highest temperatures.

number density needs to be accurately calculated; this is performed with a second series of lookup tables that contain the electron-to-ion ratio of each wind across a temperature range of 10^4 to 10^9 K (figure 4.3). The electron number density is found to be $n_e = \beta n_i$ where β is the electron-to-ion ratio and n_i is the ion number density. Another difference between calculating electron-grain and gas-grain cooling is calculating electron-grain transparency, which is a significantly more complex problem than calculating ion-grain transparency. An assumed full opacity proves to be extremely inaccurate at temperatures $> 10^6$ K. Electron-grain transparency is therefore calculated via an approximation described in Dwek and Werner (1981):

$$\begin{aligned} h(x^*) &= 1, & x^* > 4.5, \\ &= 0.37x^{*0.62}, & x^* > 1.5, \\ &= 0.27x^{*1.50}, & \text{otherwise,} \end{aligned} \tag{4.10}$$

where $x^* = 2.71 \times 10^8 a^{2/3} (\mu\text{m}) / T$. This approximation is approximately 4 orders of magnitude faster than using an integration method, while only being out by $\sim 8\%$ in the worst case scenario (figure 4.4). Grain-grain collisions are not modelled, as this would be difficult to calculate due to the single-fluid model in use. Further simulations utilising a multi-fluid model could allow for this to be simulated.

4.2.2 Numerical modelling of dust through advected scalars

The most important modification to Athena++ was the addition of a dust growth and destruction model to simulate the production of dust within the WCR. A passive scalar model was used where dust can evolve and advect through the simulation, analogous to a co-moving fluid, which previous papers have noted is an accurate dynamical model for dust within the WCR (Hendrix et al., 2016). In these simulations, dust is stored in the form of two variables, the average grain radius, a , and the dust-to-gas mass ratio, z . From these constants the dust production rate, number density, and total dust mass can be derived. A co-moving model allows for a simplified model of dust formation. In such a model, the mean particle velocity between two particles of different size can be given as:

$$\langle u \rangle = \left[\frac{8kT}{\pi m_r} \right]^{1/2}, \quad (4.11)$$

where m_r is the familiar reduced mass between a test particle of mass m_t and a field particle of mass m_f

$$m_r = \frac{m_f m_t}{m_f + m_t}. \quad (4.12)$$

As the dust grain is significantly more massive, the reduced mass is approximately equal to the grain mass, simplifying the dynamics of the simulation in a co-moving case. Dust growth is modelled through approximating growth due to grain-gas accretion where grains co-moving with a gas perform relatively low-velocity collisions with the surrounding gas, causing it to accrete onto the surface of the dust grain (Spitzer Jr., 2008). Assuming a single average grain size the change in average grain radius is given by

$$\frac{da}{dt} = \frac{\xi_a \rho_{Gr} w_a}{4\rho}, \quad (4.13)$$

where w_a is the Maxwell-Boltzmann distribution RMS velocity, ξ_a is the grain sticking efficiency and ρ_{Gr} is the grain bulk density. The associated rate of dust density change is found to be

$$\frac{d\rho_D}{dt} = 4\pi a^2 \rho_g n_D \frac{da}{dt}, \quad (4.14)$$

where ρ_g is the gas density and n_D is the grain number density. In this paper ξ_a is assumed to be 10% while a bulk density analogous to amorphous carbon grains of 3 g cm^{-3} is utilised.

4. A PARAMETER SPACE EXPLORATION OF DUST FORMATION

Dust destruction is calculated via gas-grain sputtering using the Draine and Salpeter (1979) prescription - a dust grain has a lifespan, τ , which is dependent on the grain radius. Assuming a spherical grain, the rate of change in mass and radius can be calculated such that:

$$\tau_D = 1 \text{ Myr} \times \frac{a}{n_g}, \quad (4.15a)$$

$$\frac{da}{dt} = -\frac{a}{\tau_D}, \quad (4.15b)$$

$$\frac{dm}{dt} = -1.33 \times 10^{-13} a^2 n_g n_d \rho_{Gr}, \quad (4.15c)$$

where n_g is the gas number density.

In order to propagate dust through each simulation, a small initial value for the advected scalars is set in each cell in the remap zones. A minimum grain radius of 50 Å and minimum dust-to-gas mass ratio of 10^{-6} is imposed. Changing z_{min} does not significantly impact the final dust-to-gas mass ratio of the system as z rapidly increases within the WCR and dust growth in the WCR dominates the total production.

4.3 Model Parameters

In this paper we do not intend on modelling particular systems. Rather we intend to gain a deeper understanding of what the primary influences of dust formation are in a CWB system. A series of simulations were therefore run in order to determine how dust formation varies due changes in orbital separation and wind momentum ratio. A baseline simulation with properties similar to WR98a with a circular orbit and identical stellar masses was created. Additionally, this baseline simulation has a momentum ratio of 0.02. Other simulations were then run with different orbital separations and/or wind momentum ratios. Another set of simulations were run where the cooling mechanisms were selectively disabled, in order to understand how radiative cooling effects the dust production rate. Table 4.2 and 4.3 detail the wind and orbital parameters of the baseline simulation. The orbital separation is modified by changing the orbital period of the simulation, while wind momentum ratio is modified by adjusting the mass loss ratio and wind terminal velocity for each star. Two simulation sub-sets for this were performed, simulations where the wind terminal velocities were adjusted for each star and simulations where the mass loss rates for each star were adjusted.

Parameter	WR	OB	Unit
\dot{M}	5.0×10^{-6}	5.0×10^{-8}	$M_{\odot} \text{ yr}^{-1}$
v_{∞}	1.0×10^8	2.0×10^8	cm s^{-1}
T_w	1.0×10^4	1.0×10^4	K

Table 4.2: Wind properties of the baseline system.

Parameter	Value	Unit
M	10.0	M_{\odot}
d_{sep}	4.0	AU
P	1.80	yr

Table 4.3: Baseline system orbital properties.

4.3.1 Cooling mechanisms

For this set of simulations, the influence of cooling was changed by varying how cooling works within the simulations. All simulations in this set keep the same orbital and wind parameters, which are that of the baseline system described in tables 4.2 & 4.3. One simulation has both plasma and dust cooling in operation (the `fullcool` simulation), while the other two simulations have plasma cooling only and no cooling respectively (`plasmacool` and `nocoool`, table 4.4). The final, no radiative cooling simulation instead relies on adiabatic expansion for temperature change; as such, this simulation behaves as if it has a χ value for both winds that is arbitrarily high. The post-shock flow in the `nocoool` model will also be unable to compress as much due to the lack of energy loss via radiative cooling. The role of these simulations is to discern whether it is cooling alone or other system parameters that affects dust production.

Name	Plasma cooling	Dust cooling
<code>fullcool</code>	Yes	Yes
<code>plasmacool</code>	Yes	No
<code>nocoool</code>	No	No

Table 4.4: Cooling series simulation parameters

4. A PARAMETER SPACE EXPLORATION OF DUST FORMATION

Name	\dot{M}_{WR}	\dot{M}_{OB}	v_{WR}^∞	v_{OB}^∞	η	χ_{WR}	χ_{OB}
	$M_\odot \text{ yr}^{-1}$	$M_\odot \text{ yr}^{-1}$	cm s^{-1}	cm s^{-1}			
baseline	5.0×10^{-6}	5.0×10^{-8}	1×10^8	2×10^8	0.02	1.20	1915
mdot-1	1.0×10^{-5}	5.0×10^{-8}	1×10^8	2×10^8	0.01	0.60	1915
mdot-2	2.5×10^{-6}	5.0×10^{-8}	1×10^8	2×10^8	0.04	2.39	1915
mdot-3	5.0×10^{-6}	1.0×10^{-7}	1×10^8	2×10^8	0.04	1.20	957
mdot-4	5.0×10^{-6}	2.5×10^{-8}	1×10^8	2×10^8	0.01	1.20	3830

Table 4.5: Wind parameters for simulations varying the mass loss rate, \dot{M} .

4.3.2 Wind momentum ratio

Another set of simulations was devised in order to assess the influence of the wind parameters on the formation of dust within a CWB. As the wind momentum ratio is dependent on both the mass loss rate and wind velocity of each star, each of these properties is modified over a course of simulations. η is varied from 0.01 to 0.04 by adjusting the wind parameters for each star. This is further subdivided by which property is modified, either the mass loss rate (table 4.5) or wind terminal velocity (table 4.6). As the cooling parameter has a much stronger dependency on v_∞ than \dot{M} , the modification of either parameter while maintaining a similar value for η allows us to determine whether the cooling parameter is the primary characteristic determining the formation of dust within WCd systems. This can be seen when comparing simulations mdot-1 and vinf-1, which have similar wind momentum ratios but the cooling parameters for the WC star differ by a factor of 32. These simulations are compared to the baseline simulation, which a radiative post-shock WCR. Whilst the simulations with $\eta = 0.00$ still have very imbalanced winds, they are typical of a WR+OB binary with a less intense Wolf-Rayet partner star wind. All simulations were run for a minimum of 1 orbit. As these orbits are circular, there should be no major variance of the winds after the start-up transients are fully advected, save for some fluctuations.

4.3.3 Separation distance

A final series of simulations was performed with the wind parameters equivalent to the baseline model, but with differing orbital separations. The separation was altered by modifying the orbital period of each star, as stellar masses were to be kept realistic. The separation distance was varied from the baseline model of 4 AU to 64 AU (table 4.7), which has the effect of modifying

4.3 Model Parameters

Name	\dot{M}_{WR}	\dot{M}_{OB}	v_{WR}^∞	v_{OB}^∞	η	χ_{WR}	χ_{OB}
	$M_\odot \text{ yr}^{-1}$	$M_\odot \text{ yr}^{-1}$	cm s^{-1}	cm s^{-1}			
baseline	5×10^{-6}	5×10^{-8}	1×10^8	2×10^8	0.02	1.20	1915
vinf-1	5×10^{-6}	5×10^{-8}	2×10^8	2×10^8	0.01	19.1	1915
vinf-2	5×10^{-6}	5×10^{-8}	5×10^7	2×10^8	0.04	0.07	1915
vinf-3	5×10^{-6}	5×10^{-8}	1×10^8	4×10^8	0.04	1.20	30638
vinf-4	5×10^{-6}	5×10^{-8}	1×10^8	1×10^8	0.01	1.20	120

Table 4.6: Wind parameters for simulations varying the wind terminal velocity, v^∞ .

the cooling parameter of each simulation without changing the wind momentum ratio; allowing us to further discern which is the dominant parameter influencing dust formation. For instance, simulation **dsep-64AU** has a cooling parameter value approaching the fast WR wind model **vinf-1**, despite having a wind momentum ratio of 0.02.

Each simulation has a coarse resolution of $320 \times 320 \times 40$ cells, with a varying number of levels, as the separation distance is doubled, the associated static mesh refinement box is halved and the number of levels is decremented. This manipulation of levels ensures that the number of cells between the stars is kept consistent, reduces memory usage and keeps the average timestep approximately the same. The simulation extent was doubled over the previous simulations, to approximately $2000 \times 2000 \times 250$ AU. Similarly to the previous set of simulations, a minimum of 1 orbit was needed for each simulation, however, as the orbital period of each simulation varies, certain simulations were able to run for a significantly longer length of time, with data for multiple orbits being obtained.

Name	P	d_{sep}	χ_{WR}	χ_{OB}	Levels	Effective Resolution
						Cells
dsep-4AU	1.80	4	1.20	1915	7	$20480 \times 20480 \times 2560$
dsep-8AU	5.06	8	2.39	3830	6	$10240 \times 10240 \times 1280$
dsep-16AU	14.3	16	4.79	7659	5	$5120 \times 5120 \times 640$
dsep-32AU	40.5	32	9.57	15319	4	$2560 \times 2560 \times 320$
dsep-64AU	115	64	19.1	30638	3	$1280 \times 1280 \times 160$

Table 4.7: Parameters of simulations varying separation distance.

4. A PARAMETER SPACE EXPLORATION OF DUST FORMATION

4.3.4 Data collection

Data was collected in multiple forms. HDF5 files were generated at regular time intervals - 3D HDF5 meshes were generated every 1/100th of an orbit, while 2D slices were produced every 1/1000th of an orbit. These HDF5 files contain the primitive variables of the simulation, gas density, ρ , gas pressure, P and wind velocity components, v_x , v_y and v_z ; these can be used to derive other variables such as the gas temperature as well as the internal, kinetic and total energies. The scalars governing the dust properties were also stored for each cell, the dust-to-gas mass ratio, z and the dust grain radius, a . The wind “colour” was also tracked. This is the proportion of gas resultant from each star; a value of 1.0 is a pure WR wind, 0.0 is a pure OB wind, while 0.5 is a perfectly mixed wind. In addition to HDF5 outputs, the volume-weighted summations of all system parameters, such as the total system mass and summated average grain radius were collected. In order to derive average values, such as \bar{z} and \bar{a} , the values for each can be divided by the total system mass. To calculate dust formation within the WCR, a method of determining if a cell was a part of the wind collision region was devised - the cell density would be compared to the predicted density of a single smooth wind with the wind parameters of the Wolf-Rayet star in the system:

$$\rho_{\text{SW}} = \frac{\dot{M}_{\text{WR}}}{4\pi r^2 v_{\text{WR}}^\infty}, \quad (4.16)$$

where r is the distance from the barycentre. This threshold value was set to $1.25\rho_{\text{SW}}$ as it most accurately determined if a cell was part of the WCR. Increased threshold values were not accurate at large distances from the barycentre (figure 4.5). Other methods of detecting the Wind Collision Region such as determining wind mixing levels were not successful in general. A mixed wind model for detecting over-density was also considered, however it was not any more accurate than the single wind over-density model.

4.4 Results

4.4.1 Radiative processes

The first round of simulations were performed in order to assess whether the implemented cooling model would influence dust formation within the WCR. This was found to be the case, figure 4.8 shows that without cooling only a marginal amount of dust formation occurs, largely due to propagation of dust grains into the simulation, dust destruction also appear to be occurring,

4.4 Results

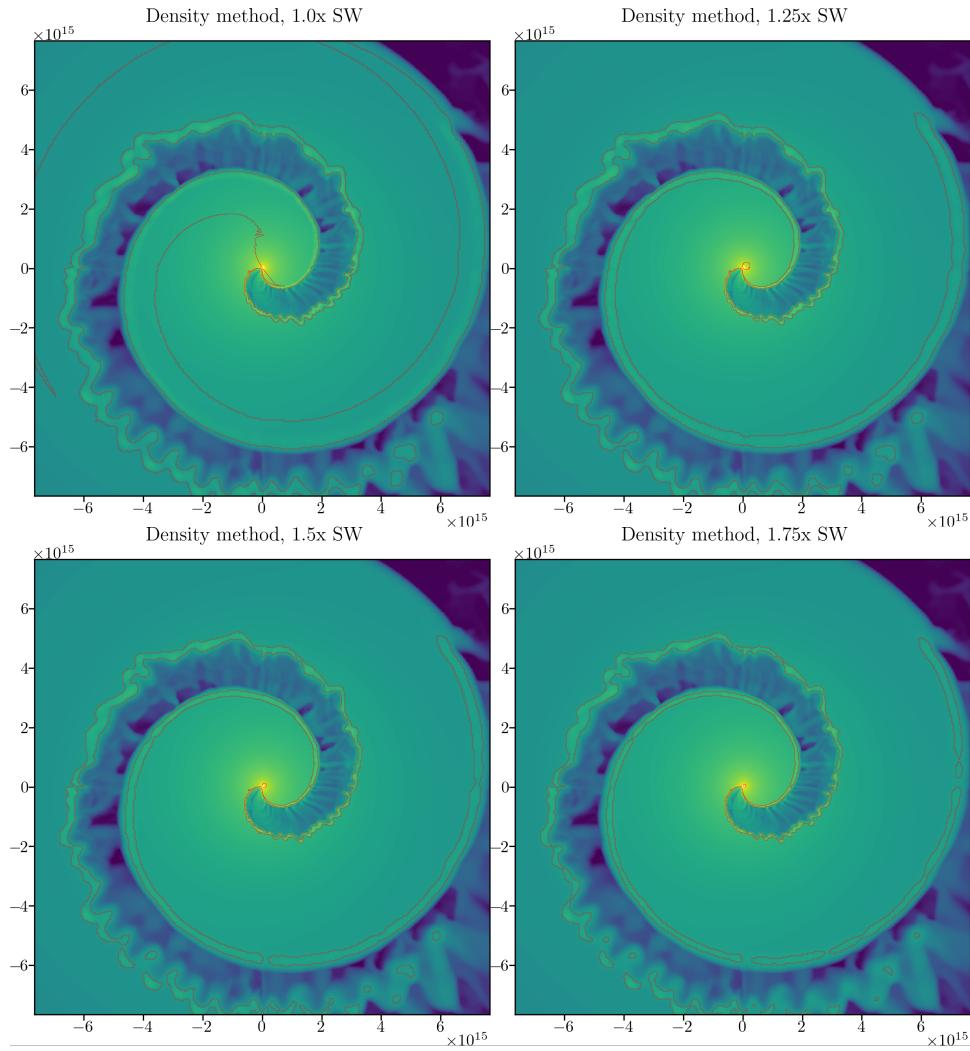


Figure 4.5: Comparison of threshold values for the over-density method of determining if a cell resides in the wind collision region. A threshold value of $1.25\rho_{SW}$ was chosen as it most accurately determined if the cell was in the post-shock region.

4. A PARAMETER SPACE EXPLORATION OF DUST FORMATION

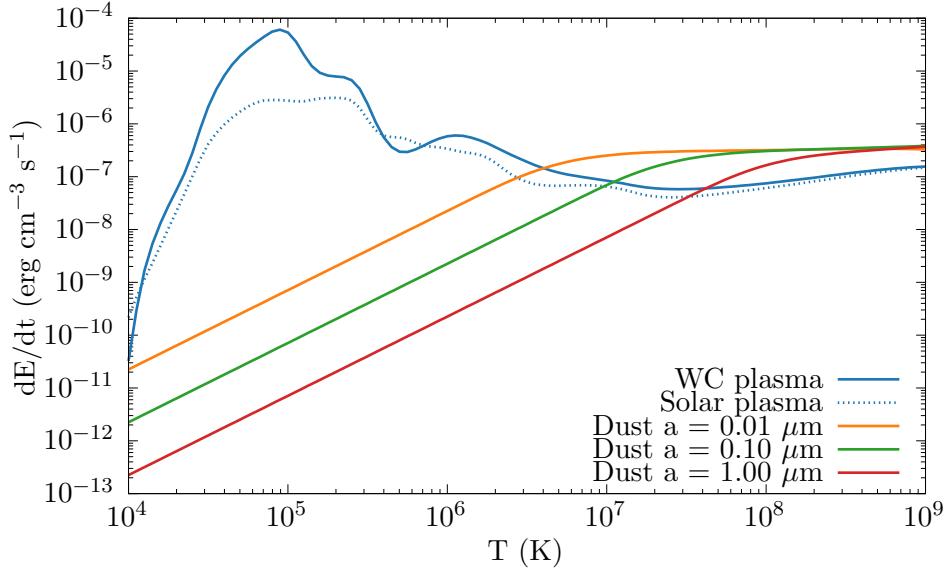


Figure 4.6: Comparison of plasma cooling to dust cooling with varying grain sizes in a typical post-shock flow, where $\rho_g = 10^{-16} \text{ g cm}^{-3}$ and a dust-to-gas mass ratio of 10^{-4} .

with the average grain radius radius reducing over the course of the simulation. Dust production for the radiative processes simulations is significantly higher, with the `fullcool` simulation appearing to have consistently higher dust formation rates than `plasmacool`. This is sensible, as 4.6 shows that at immediate post shock temperatures small dust grains present strongly influence immediate post-shock cooling, allowing the wind to reach temperatures low enough for dust formation faster than if only plasma cooling was considered.

In the case of the `fullcool` simulation, an average dust production rate of $5.4 \times 10^{-10} M_{\odot} \text{ yr}^{-1}$ is observed, with a peak formation rate of $7.1 \times 10^{-9} M_{\odot} \text{ yr}^{-1}$, this fluctuation appears to be due to dust forming mostly in high density instabilities (figure 4.8). The fluctuations occur multiple times per orbit, but do not appear to be related to the orbital motion itself.

As cooling is significant in the post-shock WR wind, non-adiabatic compression is allowed to occur, resulting in much higher post-shock densities (figure 4.9). Gas rapidly cools within this post-shock region, corresponding to where energy losses were stated to be important in Usov (1991), this results in ideal conditions for dust formation, especially within the higher density instabilities. A similar effect for the OB wind is not observed, as radiative energy losses are not influential on the dynamics of the flow, due to the faster, significantly thinner stellar wind. Figure 4.10 shows that the `fullcool` simulation has a similar immediate-post shock temperature

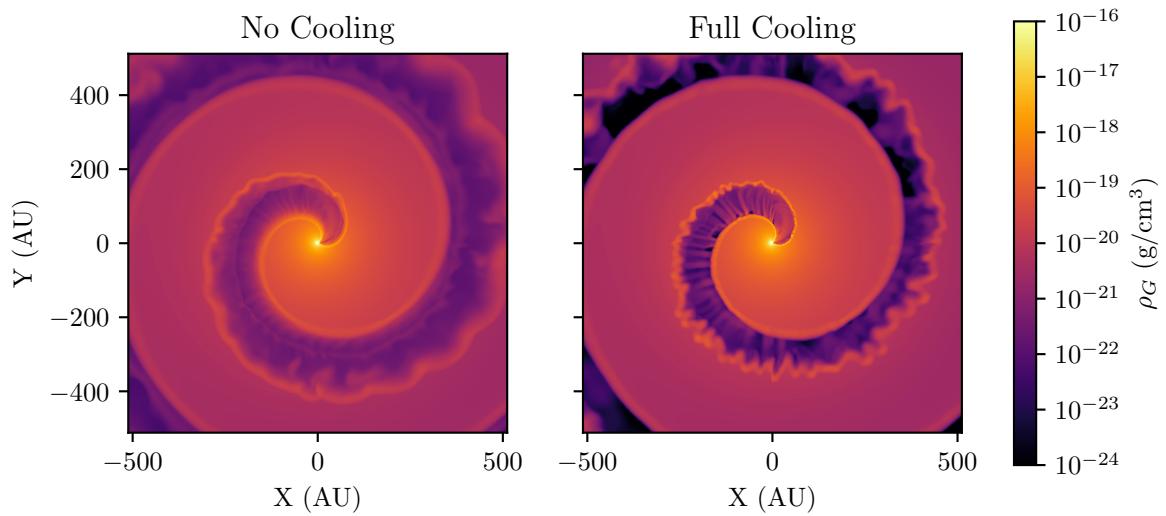


Figure 4.7: Density comparison for `nocool` and `fullcool` models, with cooling enabled instabilities are far more prevalent, with pockets of very high density material within the WCR.

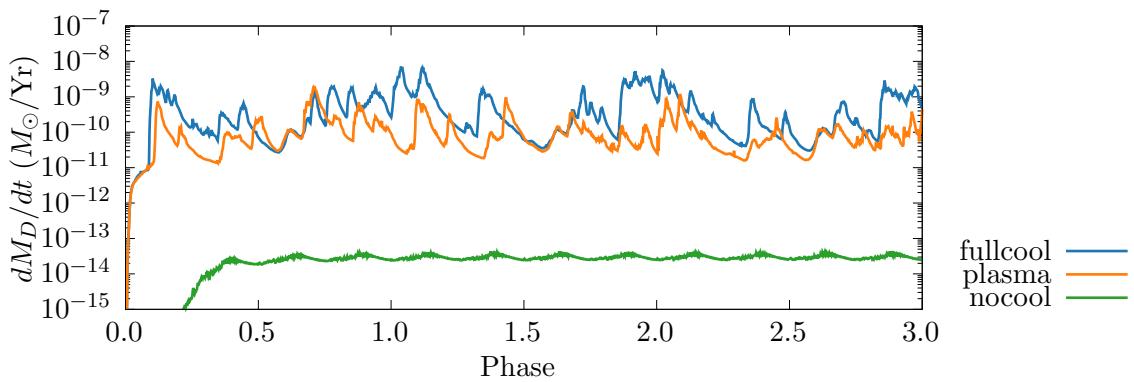


Figure 4.8: A comparison of dust formation rates as cooling mechanisms are changed. Without adequate cooling barely any dust is formed, while dust formation does increase with all cooling mechanisms enabled plasma cooling is still the dominant cooling process for dust production.

4. A PARAMETER SPACE EXPLORATION OF DUST FORMATION

to an adiabatic model, however this region cools within an extremely short timescale, allowing the nascent dust grains to grow. Figure 4.11 shows dust clumps forming shortly after initial wind collision, these clumps rapidly convert post-shock gas to dust, after a short period of time, however, this dust production tapers off as the post-shock wind becomes more diffuse. This behaviour is similar to previous models, which suggest that the bulk of dust formation occurs only a short distance from the parent stars. Temperature is also significantly more affected in the leading edge relative to the orbital motion, leading to a larger portion of dust forming in this region.

Pittard (2009) notes that in the case of colliding winds with $\eta = 1$ the trailing edge of the WCR takes part in oblique shocks with the stellar winds, while the leading edge is shadowed by the upstream WCR from the colliding material. This results in a trailing edge with strong instabilities and cool, high density clumps of post-shock wind, while the leading edge has a low density flow that is not dominated by instabilities. This does not appear to occur in these low- η systems, as oblique shocks occur at a much greater distance, when the stellar wind is significantly less dense. Instead, the leading edge of the WCR appears to be much thinner and denser than the trailing edge, this is believed to be due to the leading edge interacting with the outflowing material due to the systems orbital motion, sweeping up material and obliquely shocking the downstream WCR. Most dust formation occurs in the downstream post shock region, as soon as the post-shock wind has sufficiently cooled. Furthermore dust formation slows significantly as the post-shock wind begins to diffuse, limiting overall dust formation to a region around 100 AU from the WCR apex. This is in agreement with the research by Williams et al. (1990) and Hendrix et al. (2016), which note that there is a limited region suitable for dust formation.

4.4.2 Mass loss rate variation

Dust formation in the set of simulations which vary mass loss rate was found to be dependent on strong winds from either the WC or OB stars. As can be seen in figure 4.12, the rates are stratified into similar dust production rates for simulations with similar values of η ; simulations with an η of 0.01 produce the most dust, while simulations with $\eta = 0.04$ producing approximately 3 orders of magnitude less dust than the most productive simulations. However, the heightened dust production rate does not correspond to the summated mass loss rate of the system. For instance, `mdot-1` and `mdot-3` produce on average $\sim 10^{-8} M_{\odot} \text{ yr}^{-1}$ with a net mass loss rate with factors of 1.99 and 1.01 higher than the baseline simulation respectively. While the mass loss rate for each star varies throughout these simulations by a factor of 4, the dust

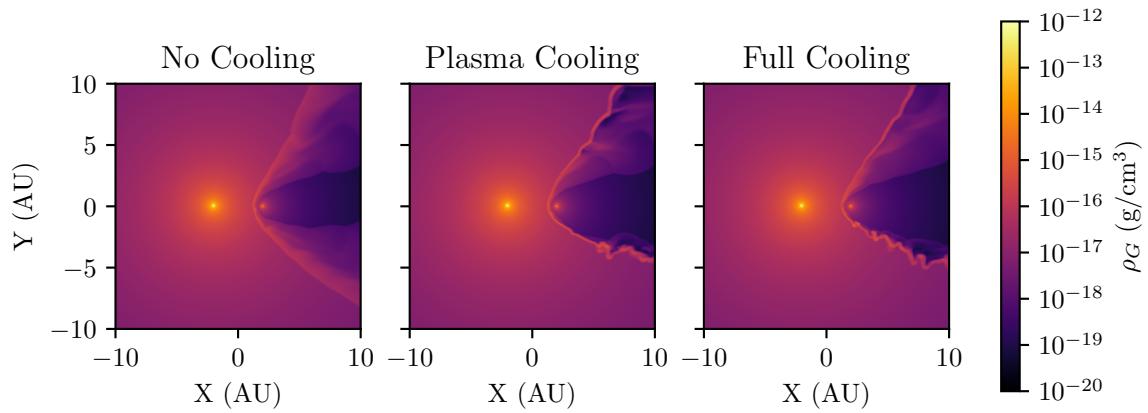


Figure 4.9

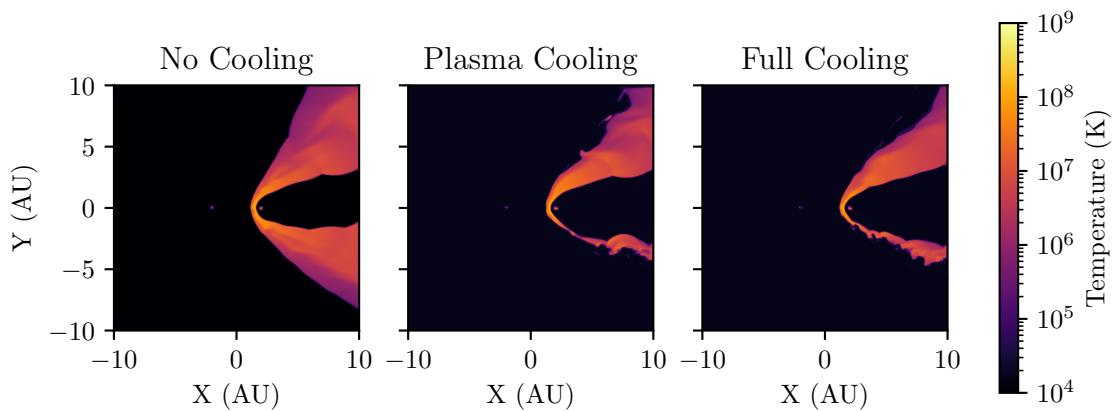


Figure 4.10

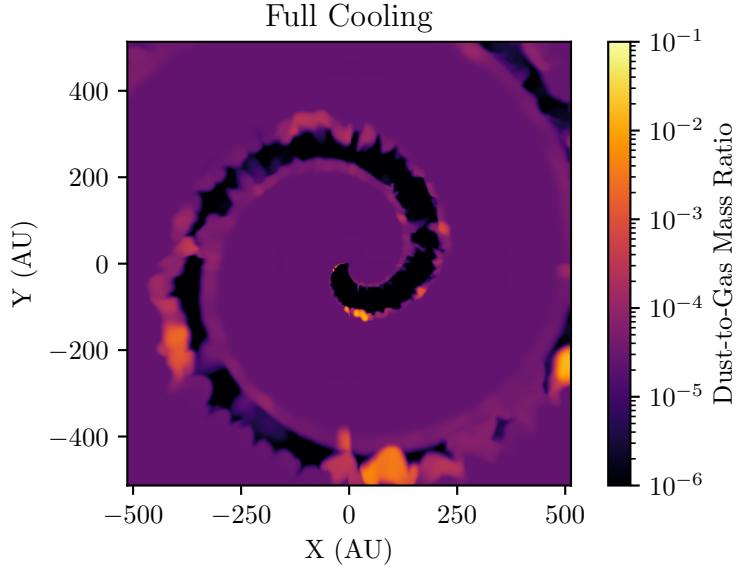


Figure 4.11: Full extent of baseline simulation, showing dust-to-gas mass ratio, dust typical forms in clumps within instabilities, leading to variation of dust formation as the simulation progresses.

production rate varies significantly more than that, further ruling out the increased rate of dust production being due to there simply being more mass in the simulation. All simulations in this system have comparatively low values for χ_{WR} , which suggests that the simulations are at least weakly radiative, this implies that cooling is not the only governing factor, and that a strong shock must also form.

4.4.3 Terminal velocity variation

Varying wind terminal velocity appears to have an extremely strong effect on dust formation, with effects that are not solely related to η . Dust production rate is extremely high in the case of `vinf-2`, which has an extremely slow wind velocity of 500 km s^{-1} , which is on the low end of expected wind terminal velocities for WR stars, and has a wind velocity closer to that on a typical LBV star. This very slow, dense wind is highly influenced by radiative cooling in the post-shock environment, driving thermal instabilities, leading to high density pockets of cooled gas, ideal for dust formation. This can be seen in figure 4.14, where `vinf-2` produces large quantities of dust in the WC-stagnation point interaction region, which is mixed throughout the WCR, this flow is highly radiative, and rapidly cooled back to the initial wind temperature.

4.4 Results

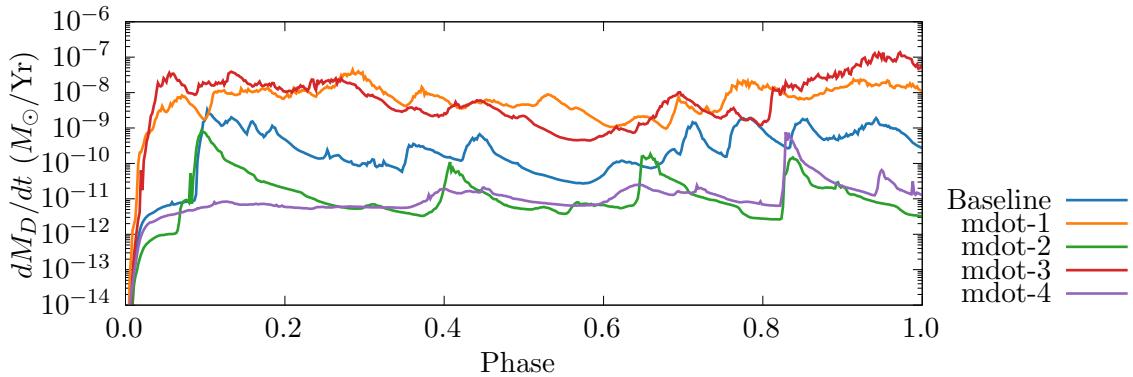


Figure 4.12: A comparison of dust production rates for simulations that vary mass loss rate, \dot{M} , simulations with either a strong primary or secondary wind produce similar levels of dust, whilst if either wind is weaker, dust production rate is reduced.

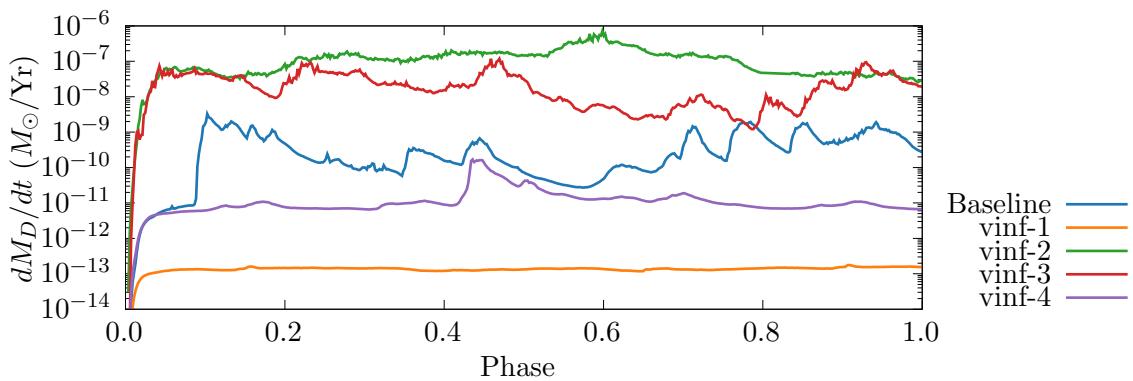


Figure 4.13: Comparison of dust production rate for simulations varying wind terminal velocity, v^∞ . Simulations

4. A PARAMETER SPACE EXPLORATION OF DUST FORMATION

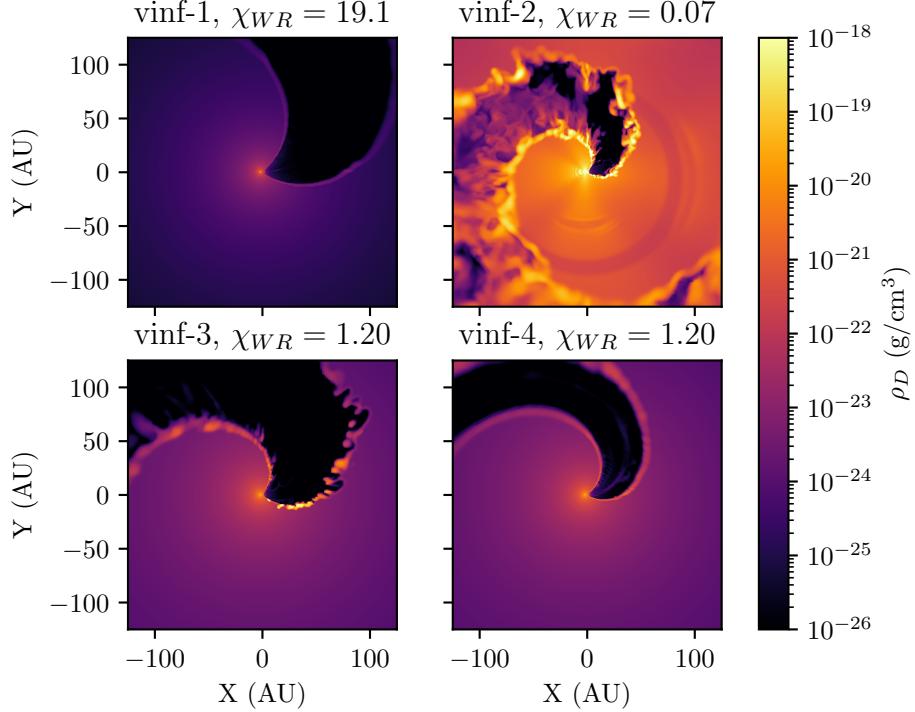


Figure 4.14: Comparison of dust density in v^∞ variation simulations, simulations with either a low OB wind velocity or high WC wind velocity produce large quantities of dust. Simulation **vinf-1**, which has a high velocity WC wind, does not produce any appreciable dust within the WCR.

the significant velocity imbalance between the primary and secondary wind (a factor of 4) suggests that a strong velocity shear may occur, leading to the formation of Kelvin-Helmholtz instabilities. It should be noted that dust production in general increased outside of the WCR in the case of **vinf-2**, this is largely due to significantly higher wind density within the WC wind, and increased formation time before wind collision. This dust would be destroyed via the photodissociation process, which is not included in this model, but would be included in future models if this avenue of research is continued. Despite this, the dust production outside of the WCR does not significantly impact the total dust production rate, and numerical analysis of dust production such as in figure 4.19 does not include dust produced outside of the wind collision region. In the case of a fast WC wind however, dust production effectively ceases, with an average dust production rate of $8.9 \times 10^{-13} M_\odot \text{ yr}^{-1}$, multiple orders of magnitude less than **vinf-4**, which has a similar wind momentum ratio.

4.4 Results

Simulations `vinf-3` and `vinf-4` are of note as when the secondary wind velocity was altered, drastic changes to the dust formation rate occur, similar to modifying the mass loss rate of the secondary star as detailed in the previous section. Instabilities due to the secondary wind appear to be the result of this, a greater secondary wind velocity would lead to a greater velocity shear along the discontinuity, resulting in Kelvin-Helmholtz instabilities. Both `vinf-2` and `vinf-3` exhibit this behaviour, and both have a terminal velocity ratio, $\frac{v_{\text{OB}}^{\infty}}{v_{\text{WR}}^{\infty}} = 4$. This would augment the already present thermal instabilities due to radiative cooling, leading to a less ordered, clumpy post-shock environment (Stevens et al., 1992). This is found to be the case with `vinf-3`, which has a far greater amount of dust formation within the WCR, and has a significantly more mixed wind. This can be seen in figure 4.15 where `vinf-3` and `vinf-4` are directly compared, despite both simulations having an adiabatic second wind, the presence of a much faster secondary wind results in a velocity shear that produces a much broader WCR, with high density pockets formed within instabilities, which appear to produce the bulk of dust. This suggests that prolific dust formation occurs in a post-shock primary wind shaped by instabilities, produced either from strong radiative cooling, or through a strong velocity shear, leading to K-H instabilities. Radiative cooling is also important beyond thermal instabilities, in order to reduce to adequate temperatures in the high-density immediate post shock flow. Results appear to be stratified somewhat in terms of η , where simulations where $\eta = 0.04$ produce significantly more dust than simulations with more imbalanced winds. However, this dependence is different to the mass loss rate simulation subset, and the stratification is less apparent, this suggests a loose correlation between \dot{M}_D and η when v_{∞} is varied.

By directly comparing two prolific dust producing models with $\eta = 0.04$, `vinf-3` and `mdot-3`, we can see that both WCRs are dominated by instabilities. `vinf-3` in particular appears to be much more thoroughly mixed (figure 4.16), with a much larger trailing edge that produces large quantities of dust (figures 4.17). This additional degree of instability appears to be due to Kelvin-Helmholtz instabilities, which grow significantly as the post-shock gas flows away from the stagnation point, as described in Stevens et al. (1992). These simulations produce approximately the same amount of dust, with `vinf-3` also consistently producing dust in the trailing edge of the WCR. From these results it is clear that a high dust production rate is dependent on a highly imbalanced wind, with a slow WC and fast OB wind, as this drives a strong shock, leading to strong cooling and thin-shell instabilities, while also producing additional high density regions and mixing through Kelvin-Helmholtz instabilities.

4. A PARAMETER SPACE EXPLORATION OF DUST FORMATION

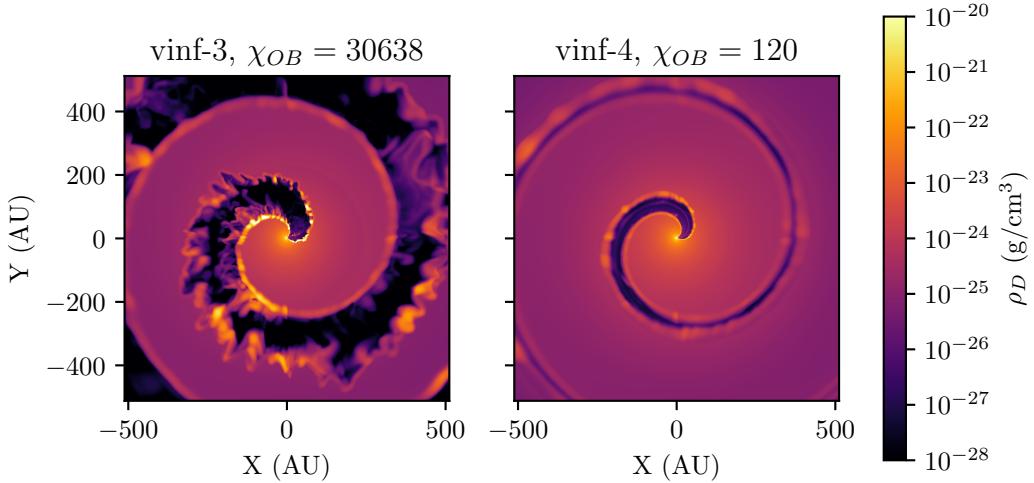


Figure 4.15: Comparison of dust density in simulations with at modified OB wind terminal velocities, simulations are fully advected with $\phi = 3.0$, dust formation and instabilities are far more pronounced in **vinf-3**, which has wind velocity a factor of 4 larger than **vinf-4**.

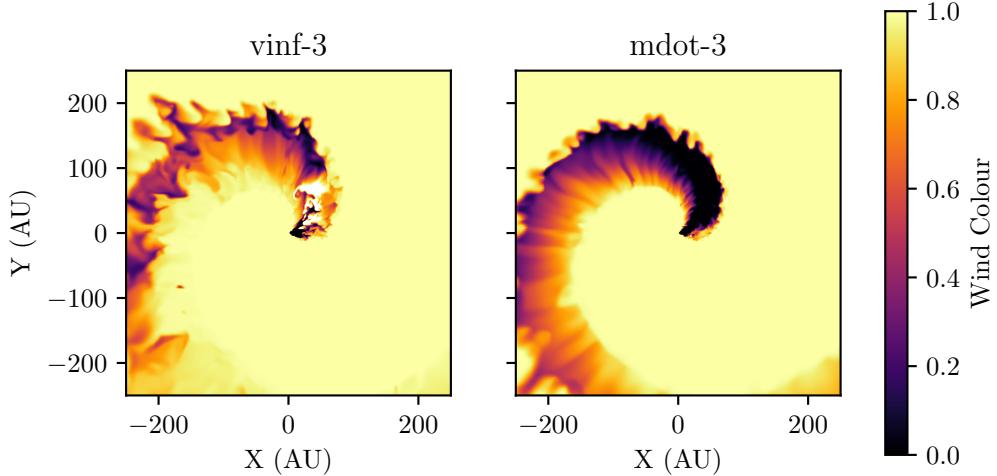


Figure 4.16: Comparison of wind colour in simulations **vinf-3** and **mdot-3**, wind mixing is significantly more pronounced, with a pronounced post-shock WR wind that appears to be strongly influenced by Kelvin-Helmholtz instabilities, due to the increased wind velocity imbalance and lower degree of cooling.

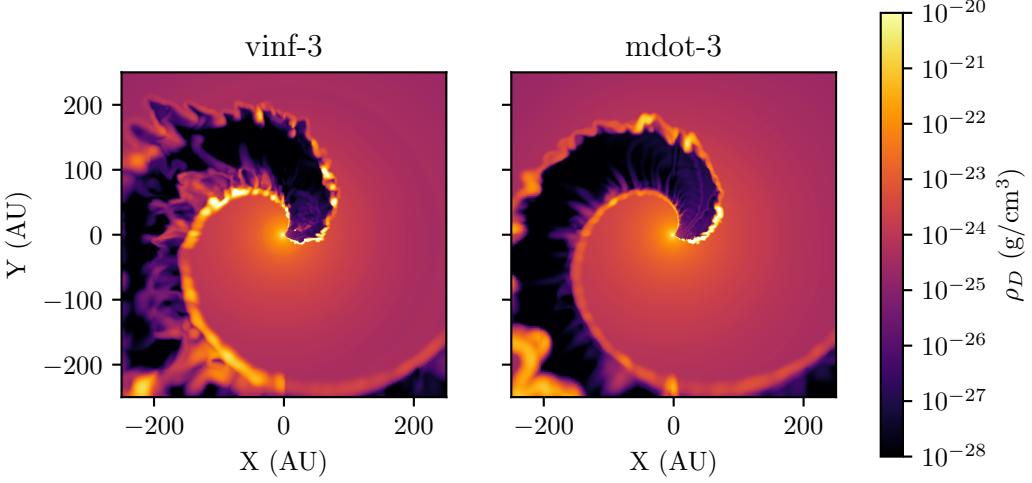


Figure 4.17: Comparison of dust density in simulations with a strong secondary wind, `vinf-3` & `mdot-3`, dust in `vinf-3` is produced to a much higher degree in the trailing edge of the wind, and increased mixing of the wind due to Kelvin-Helmholtz instabilities has led to dust forming throughout the WCR, rather than at the WC-stagnation point boundary.

4.4.4 Separation variation

As can be seen in figure 4.19 there is a clear correlation between separation distance and dust formation rate, with dust production drastically increasing as orbital separation is decreased. This influence on the dust formation rate is non-linear, with a doubling of the separation distance increasing the dust production rate by approximately one order of magnitude. Variation of the dust production rate also appears to increase as separation distance is reduced, leading to instances where a simulation may temporarily produce more dust than a simulation with a tighter orbit, such as the case with `dsep-4AU` and `dsep-8AU` at $\Phi = 0.6 - 0.7$. As we have previously discussed, instabilities drive slightly intermittent, but highly effective dust formation, which would explain this phenomena.

A clear trend with orbital separation is that dust formation increases drastically as the stars are positioned closer together, at high degrees of separation dust formation ceases, and average grain size drops below the initial value of 50Å. The bulk of dust growth occurs in the immediate post shock region, as dust is rapidly cooled and at a high enough density for dust formation to occur. This matches observations of episodic dust forming systems, where infrared emission due

4. A PARAMETER SPACE EXPLORATION OF DUST FORMATION

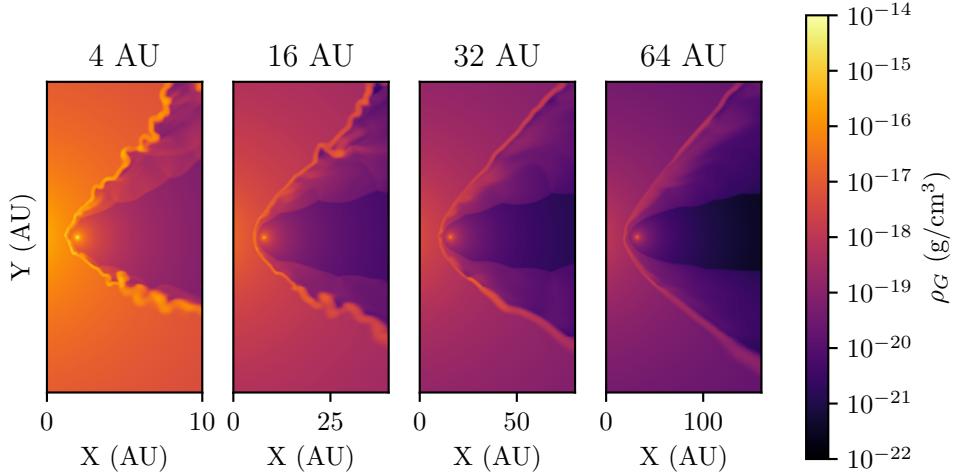


Figure 4.18: A comparison of the structures of simulations varying d_{sep} , the scale of each plot has been changed to allow for a similar feature size, as can be seen simulations with a closer separation distance have collision regions whose structure is more strongly influenced by instabilities, particularly thin-shell instabilities brought on by the presence of radiative cooling within the WCR.

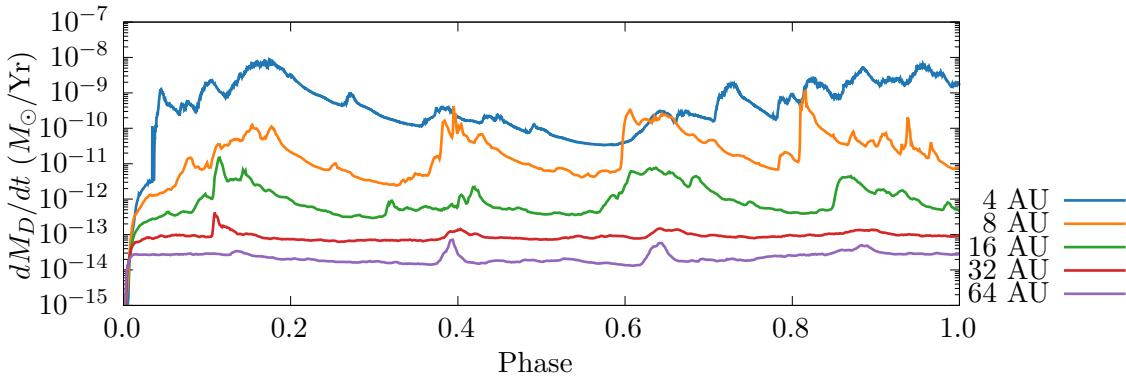


Figure 4.19: A comparison of dust formation rates versus orbital phase for a set of simulations that vary separation distance, d_{sep} . A clear inverse relationship between separation distance and dust production rate exists, most likely due to the stellar winds becoming more diffuse further from their origin stars, leading to weaker shocks and a WCR that behaves more adiabatically.

to dust is maximised at or shortly after periastron passage. This also lends further evidence that dust formation rates are not influenced solely by the momentum ratio, as this is kept constant, and instead is strongly influenced by the wind density at collision and post-shock cooling.

4.5 Conclusions

4.5.1 Dust formation sensitivity

The simulations in this paper were conducted over a fairly limited range of initial conditions for mass loss rate and wind terminal velocity, wind velocity and mass loss rates are varied by no more than a factor of 4. Despite this, dust production varies by up to 6 orders of magnitude, in the case of wind terminal velocity. This suggests that dust formation is extremely sensitive to the wind properties of both stars, and imposes a limited parameter space for dust to form in appreciable amounts. This would explain why these dust forming systems are so comparatively rare, compared to the total number of systems with binary massive stars and interacting winds; as well as why periodic dust forming systems have eccentric. Dust formation rate also varies in accordance with the separation distance, but is somewhat less sensitive to change, this would present itself more in terms of WCd systems that exhibit periodic dust formation, as WC stars do not undergo significant variability of their wind properties over the timescale observed in periodic WCd systems. This would present an interesting factor in the case of CWB systems with an LBV partner such as η Carinae, as an LBV would result in a highly variable wind collision region outside of fluctuations due to separation distance (Nazé et al., 2018). The baseline system, WR98a, has a significantly lower mass loss rate than other well-characterised WCd systems, such as WR140 and WR04, the WC star in WR 140 has a mass loss rate an order of magnitude larger than WR98a, for instance. As such, future research in this topic will cover these systems, as an exploration of more extreme conditions would be conducive to demonstrating the veracity of this dust model.

4.5.2 Radiative inhibition and its influence on eccentric WCd systems

The lack of radiative line driving, and instead using a terminal velocity model for stellar winds is an important consideration when assessing the results of this paper. It has been established over the course of this paper that dust production rate is highly dependent on the wind velocity of either stars stellar wind; hence any mechanism that influences the wind velocity over the course of an orbit can be a potential mechanism for the variable dust formation in CWB systems with

4. A PARAMETER SPACE EXPLORATION OF DUST FORMATION

high eccentricities. Whilst orbital separation is a definite factor in changing dust formation rates, with tightly bound orbits producing the most dust, it can be argued that as stellar separation decreases as the stars approach periastron, dust production will increase, and taper off as the star moves beyond this point as it heads towards apastron. This can be seen in observations, as dust production reaches its peak at periastron passage, however, dust formation ramps up extremely rapidly, whilst taking much longer to reduce (Williams, 2008; Williams et al., 2009). This asymmetry implies processes that occur more strongly as the system heads towards periastron than away from it. Changes to wind velocity may prove to be a source of mechanisms behind this effect.

As the wind is highly imbalanced, the velocity of the OB stellar wind will be lower than the expected terminal velocity due to insufficient acceleration before the wind undergoes radiative inhibition and braking. Whilst dust formation benefits from a slow primary wind, a slow secondary wind can drastically reduce the rate of dust formation. For instance, in the case of WR 140 at periastron passage, the O4-5 companion star with a terminal wind velocity of 3200 km s^{-1} was found to have a line-driven wind velocity $\sim 84\%$ of v^∞ before collision with the WCR at r_{OB} (figure 4.20). As demonstrated in the velocity variation simulations, halving the wind terminal velocity can reduce the dust formation rate by approximately 2 orders of magnitude, due to a weaker wind collision shock and a reduction in instabilities. A reduction of 84% in the secondary wind velocity with no corresponding reduction in the primary wind velocity would result in a noticeably lower overall dust production rate for a brief period, and may be a potential factor for the rapid onset and slow decline of dust production after periastron passage.

4.5.3 Wind mixing within the WCR

While interaction between Hydrogen and dust grains is not simulated by the dust model, Le Teuff (2002) notes that Hydrogen could be a potential catalyst for amorphous carbon grain formation. Figure 4.21 shows that the wind is far more effectively mixed by instabilities if it is sufficiently radiative, an improved dust model which can calculate grain yields from chemical reactions could be used to investigate this further. Implementation of a chemical model into Athena++ through passive scalar is a stated goal of Athena++, though it is still in development. Additionally, a multi-wind model could be used to model the dynamics of grains, as larger grains carry significantly more than atoms in the stellar wind, and may not be necessarily co-moving in a turbulent wind environment. It should also be noted that dust formation around single WC stars has been observed, suggesting that nascent grains are formed within the WC wind, and

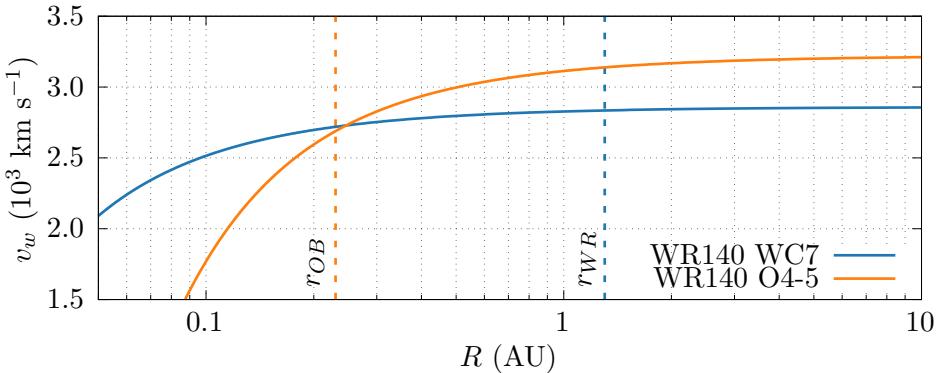


Figure 4.20: Graph of secondary wind velocity and density as a function of distance from the stellar surface due to radiative line driving for the WR 140 system, as well as an estimation of r_{OB} and r_{WR} at periastron passage. While at periastron the WC7 wind is travelling at approximately terminal velocity, the O4-5 companions wind is travelling at $\sim 84\%$ of terminal velocity before coming into contact with the WCR. CAK parameters were estimated to be $k = 0.37$, $\alpha = 0.60$ for the O4-5 star and $k = 0.48$, $\alpha = 0.57$ for the WC7 star.

carried into the Colliding Wind Binary as implied by this dust model.

4.6 Summary and Conclusions

A parameter space exploration of Colliding Wind Binary systems undergoing dust formation has proven to yield fascinating insights into how dust forms within the Wind Collision region. Dust production within these systems is poorly understood, and with direct observations of the WCR rendered difficult by the extreme conditions of these systems, it falls on numerical simulation to elucidate the post-shock conditions.

Most interesting of all is how sensitive to changing wind conditions this dust production is. The parameter space exploration, whilst quite conservative, resulted in a change in dust formation rates of up to 6 orders of magnitude over a factor of 4 change for wind velocity and mass loss rate, and a similar change in formation rate over a factor of 16 change in separation distance. In all simulations, the bulk of dust formation was found to occur within high-density pockets formed through thin-shell or Kelvin-Helmholtz instabilities, suggesting that strong cooling and a fast secondary wind both important factors for dust production. For high levels of dust formation, an ideal system should have a slow, dense primary wind, a fast, dense secondary

4. A PARAMETER SPACE EXPLORATION OF DUST FORMATION

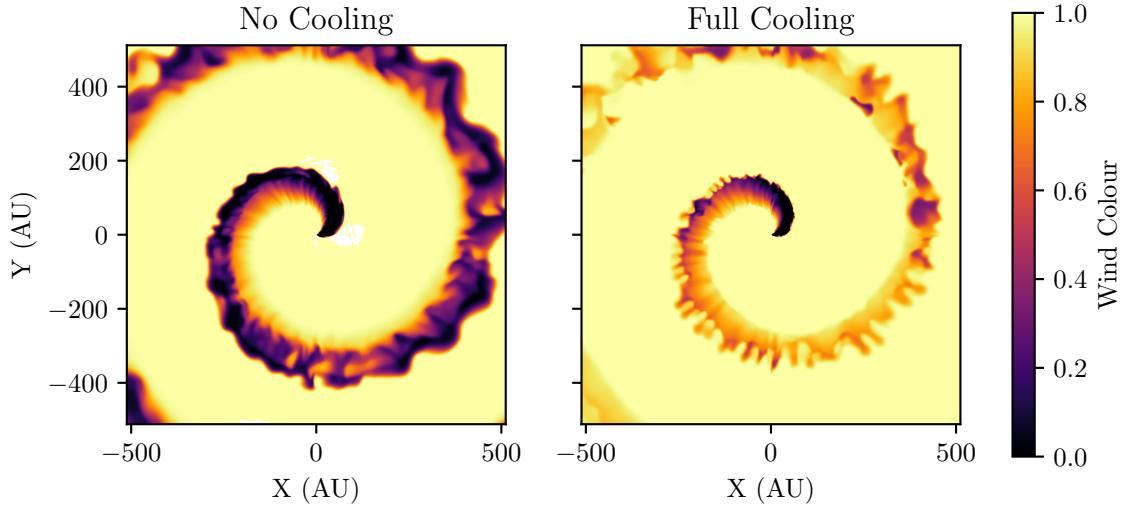


Figure 4.21: Wind “colour” for `nocool` and `fullcool` models, the WCR is more thoroughly mixed if the simulation is allowed to cool.

wind and a close orbit, a combination of these properties ensures the formation of dense pockets of cool post-shock gas ideal for formation.

There is significant room for additional research in this field, which is either in progress or a potential avenue of future research. Parameter mixing was not performed, due to the simulation time required for producing many more simulations, but performing examples on more extreme systems, such as those with a LBV primary star or a WR+WR system is a potential avenue of research. Whilst the current feature set is limited by the available remaining time in this project, future work in this vein can introduce additional dust formation and destruction mechanisms, such as grain agglomeration or photodissociation. Modelling effects such as radiative line driving or Another interesting avenue of research is the simulation of eccentric, periodic dust forming systems, as this dust model does not require manual tweaking of parameters in order to not form dust if the conditions do not permit it, running the model through a simulation of either an entire or a partial orbit of a system such as WR140 would be a logical next step for this project.

CHAPTER 5

Hydrodynamical Simulations of WCd Systems with an
Advected Scalar Dust Model

5. HYDRODYNAMICAL SIMULATIONS OF WCD SYSTEMS

Abstract

5.1 Introduction

Wolf-Rayet (WR) stars are evolved massive stars that consist of a hydrogen-depleted envelope and a highly radiative core, these stars are so luminous that the total emission from their cores is greater than the Eddington Limit, causing the envelope to be removed from the star in the form of a fast, dense stellar wind. Whilst these stars have wind velocities comparative to their less evolved and massive OB counterparts ($\sim 10^3 \text{ km s}^{-1}$) the mass-loss rate of these systems is many orders of magnitude larger ($\sim 10^{-5} M_{\odot} \text{ yr}^{-1}$).

As a majority of massive stars form in binary pairs, this can result in the fast, dense stellar wind of the WR component of the binary pair colliding with a significantly weaker stellar wind from its OB partner. This phenomena is referred to as a Colliding Wind Binary system if said phenomena plays an important role in the dynamics of the system. Observations of some of these systems have detected infrared excesses within the Wind Collision Region (WCR) which correspond with the emission from amorphous carbon dust grains. This is interesting as dust would be readily destroyed by evaporation via UV photons in the general medium, as well as the high gas temperature in the region. Instead it is believed that dust grows within the post-shock region, which rapidly cools due to the extremely high post-shock gas density. This high density region can also shield the nascent dust grains from the bulk of the photon flux from the binary stars, resulting in an ideal region for dust formation. Furthermore, this is only observed in systems where the primary star in the binary pair is a highly evolved WC9 star, this adds further complexity to the dust production problem as hydrogen depletion renders many formulation mechanisms dependent on hydrogen seeding impossible, reducing the potential yield of dust (Crowther, 2003; Williams, 2008).

Dust forming CWB systems¹ can produce upwards of $10^{-8} M_{\odot} \text{ yr}^{-1}$ of amorphous carbon dust, primarily in small grains $\sim 100 \text{ \AA}$ in radius. This can have a significant impact on the local interstellar environment in the same manner that a dust producing Asymptotic Giant Branch star can impact its surroundings. CWBd systems can be further subdivided into two types of

¹Referred to as WCd systems

5.2 Methodology

system based on their dust emission based on their dust emission rates over time, persistently forming systems and episodically forming systems¹. Based on the observations of various WCd and WCde systems there is a strong correlation between orbital eccentricity and dust production periodicity - dust forms readily at or after periastron pass, with dust production being reduced by multiple orders of magnitude at apastron (Williams & van der Hucht, 2015).

Whilst observational data of CWBd systems does exist, and dust formation can be readily observed, the distances from Earth to these systems, combined with the high levels of extinction due to the surrounding stellar wind result in it difficult to observe the dynamics of dust formation within the WCR. Instead numerical simulation of dust growth can be performed in order to discern how dust evolves in the system, this can then be compared to observations using radiative transfer modelling of the resultant numerical grids.

5.2 Methodology

Three systems were investigated for this paper, the persistent dust forming systems WR 98a and WR 104, as well as the periodic dust forming system WR 140. These systems were chosen as they have been previously been written about, and are considered archetypal dust producing CWB systems. The investigation consists of hydrodynamical modelling of the systems utilising a fork of the Athena++ hydrodynamical code, with modifications to the system in order to simulate binary system orbits, outflows and dust evolution Stone et al., 2020. Afterwards, the numerical grids produced by Athena++ are introduced into CONTINUE WHEN YOU HAVE MORE INFO ABOUT THIS

5.2.1 Hydrodynamics

3D simulations in a Cartesian coordinate system were conducted using the Athena++² hydrodynamical code,

The code solves a Riemann problem at each cell interface to determine the time-averaged values at the zone interfaces, and then solves the equations of hydrodynamics:

¹WCd

²<https://github.com/PrincetonUniversity/athena>

5. HYDRODYNAMICAL SIMULATIONS OF WCD SYSTEMS

$$\frac{\partial \rho}{\partial t} + \nabla \cdot (\rho \mathbf{u}) = 0, \quad (5.1a)$$

$$\frac{\partial \rho \mathbf{u}}{\partial t} + \nabla \cdot (\rho \mathbf{u} \mathbf{u} + P) = 0, \quad (5.1b)$$

$$\frac{\partial \rho \epsilon}{\partial t} + \nabla \cdot [(\rho \epsilon + P) \mathbf{u}] = \dot{E}_{\text{gas}} + \dot{E}_{\text{dust}}, \quad (5.1c)$$

where ρ is the mass density, $\epsilon = \mathbf{u}^2 + e/\rho$ is the total specific energy, e is the internal energy density, P is the pressure and \dot{E} is the energy loss due to radiative processes. An ideal equation of state is utilised with a ratio of specific heats, $\gamma = 5/3$.

Spatial reconstruction using a piecewise linear method was performed, while the time-integration scheme is a third-order accurate, three-stage strong stability preserving Runge-Kutta¹ method (Gottlieb et al., 2009).

Several passive scalars are utilised to model wind mixing and dust evolution, the scalar values are transported by the fluid, for a given scalar species i , Athena++ transports the scalar through the following equation:

$$\rho \frac{dC_i}{dt} = \frac{\partial}{\partial t} (\rho C_i) + \nabla \cdot (C_i \rho \mathbf{u}) = -\nabla \cdot \mathbf{Q}_i, \quad (5.2)$$

where $\mathbf{Q}_i = -\nu_{ps} \rho \nabla C_i$ is the diffusive flux density and ν is the passive scalar diffusion coefficient (Stone et al., 2020).

Stellar winds are simulated by re-writing the conserved variables in a small region around each of the stars. Winds flow from this “remap” region at the stars wind terminal velocity, meaning that line driving and stellar force effects are not simulated, additionally self-gravity forces are not simulated to reduce CPU time. The equations utilised to map wind onto the simulation are:

$$\rho_r = \frac{\dot{M}}{4\pi r^2 v_\infty}, \quad (5.3a)$$

$$P_r = \frac{\rho_r}{\mu m_H} k_B T_w, \quad (5.3b)$$

$$E_r = \frac{P_r}{\gamma - 1} + \frac{1}{2} \rho_r v_r^2, \quad (5.3c)$$

$$p_r = \rho_r v_r, \quad (5.3d)$$

¹SSPRK (3,3)

where v_R is the wind velocity as it flows radially from the center of the “remap zone” and r is the distance from the current cell to the centre of the remap zone. This method produces radially out-flowing winds from the “star” with an expected density and velocity. This method is stable against numerical instability, while allowing for precisely controlled winds.

Adaptive Mesh Refinement¹ is utilised for these simulations in order to ensure that winds form correctly and that the wind stagnation point and surrounding collision region are correctly resolved. Athena++ allows for user-defined refinement conditions, which are used in this work to increase the resolution around the stars current position as well as the estimated position of the wind stagnation point to the maximum amount, while smoothly decreasing the resolution further out from these regions.

5.2.2 Dust model and cooling

The dust model in this paper simulates dust growth and destruction through collisions between carbon atoms and dust grains. These grains are simulated in the form of advected scalars in each cell in the numerical grid which propagate with the same hydrodynamical rules as the stellar wind; as such dust can be described as co-moving with the interstellar wind. The two scalars in use are z , the dust-to-gas mass ratio within the cell, and a , the average grain radius. Using these parameters in addition to the local wind parameters, the dust can be adequately described and evolved with time.

A number of assumptions are made in this dust model, for instance, the dust grains are assumed to be spherical, with a uniform density of 3 g cm^{-3} . Dust grains are assumed to have a single size in a region, as well as a constant number density, as such, this model does not simulate grain agglomeration and fracturing. Additional mechanisms for dust formation and destruction could also be implemented such as grain-grain agglomeration and photoevaporation. Furthermore, a multi-fluid model with drag force coupling could also be implemented, however this is beyond the scope of this paper.

Dust is grown through grain accretion using formulae described by (Spitzer Jr., 2008). Dust grains grow via collisions with the surrounding gas, as gas accretes onto these grains the associated density is subtracted from the gas density. The growth rate is such that:

¹AMR

5. HYDRODYNAMICAL SIMULATIONS OF WCD SYSTEMS

$$\frac{da}{dt} = \frac{\xi_a \rho_{Gr} w_a}{4\rho}, \quad (5.4a)$$

$$\frac{\rho_D}{dt} = 4\pi a^2 \rho n_D \frac{da}{dt}, \quad (5.4b)$$

where w_a is the Maxwell-Boltzmann distribution RMS velocity, ξ_a is the grain sticking efficiency, ρ_{Gr} is the grain bulk density, ρ is the gas density, a is the dust grain radius, and n_D is the grain number density. For these simulations, the grain sticking factor has been set to 10%, while for low temperature collisions a sticking factor of 100% can be proven, grain sticking in a more energetic, hot regime could significantly reduce the probability of sticking.

Dust destruction is calculated via gas-grain sputtering using the Draine & Salpeter prescription - a dust grain has a lifespan, τ , which is dependent on the grain radius, as the grain loses radius proportional to its loss in mass; assuming a spherical grain, the rate of change in mass and radius can be calculated through the following equation:

$$\tau_D = 1 \text{ Myr} \times \frac{a}{n_g}, \quad (5.5a)$$

$$\frac{da}{dt} = -\frac{a}{\tau_D}, \quad (5.5b)$$

$$\frac{dm}{dt} = -1.33 \times 10^{-13} a^2 n_g n_d \rho_{Gr}, \quad (5.5c)$$

5.2.3 Simulated systems

The systems being simulated in this paper are the persistent dust forming systems WR 98a and WR 104, as well as the periodic dust forming system WR 140. All of these systems were selected as they are well documented, face-on systems with detailed observations in the Infrared. Additionally, these systems have a number of characteristics that are important for scientific purposes as well as for evaluation of the dust model.

WR 98a is a typical dusty CWB system that was primarily chosen for simulation as it is one of the only CWB systems whose dust dynamics have been simulated in an academic paper (Hendrix et al., 2016). The model utilised in Hendrix et al. was a dual-fluid model with an Epstein drag function in order to detail how dust flows through the system itself. As such, this model does not simulate dust accretion or cooling, and only deposits dust grains with a single set grain radius and a fixed dust production rate of $\phi = 0.0763$. However, this still provides a useful point of comparison to evaluate this papers dust model against an established model

5.2 Methodology

System	Periodic	\dot{M}_{WR} ($M_{\odot} \text{ yr}^{-1}$)	\dot{M}_{OB} ($M_{\odot} \text{ yr}^{-1}$)	v_{WR}^{∞} (km s^{-1})	v_{OB}^{∞} (km s^{-1})	η	χ_{\min}
WR 98a	No	5.0×10^{-6}	5.0×10^{-8}	900	2000	0.0222	0.7970
WR 104	No	3.0×10^{-5}	6.0×10^{-8}	1220	2000	0.0033	0.2430
WR 140	Yes	5.7×10^{-5}	1.6×10^{-6}	2860	3200	0.0314	2.6866

Table 5.1: Wind properties of systems simulated in this paper.

System	Period	Eccentricity	M_{WR} (M_{\odot})	M_{OB} (M_{\odot})	Periastron (AU)	Apastron (AU)
	(d)	(e)				
WR 98a	556	0.000	10.0	18.0	4.06	4.06
WR 104	245	0.060	10.0	20.0	2.20	2.48
WR 140	2869	0.896	14.9	35.9	1.53	26.9

Table 5.2: Orbital properties of systems simulated in this paper.

with concrete data. Furthermore, a simplified version of WR 98a was used to test the dust model and was used as a basis to explore the parameter space of dusty CWB systems by varying wind parameters and orbital separation. The parameters detailed in table 5.1 are adopted from Hendrix et al., similarly to this paper a perfectly circular orbit is assumed.

WR 104 is an archetypical dust forming binary system that is extensively observed, with multiple papers on the dynamics and formation of dust in the system.

WR 104 represents the high end of dust formation in CWB systems, with a high dust formation rate in the order of $3 \times 10^{-7} M_{\odot} \text{ yr}^{-1}$, the close separation of the binary system combined with the high mass loss rate results in a much lower value of χ for the WR wind, suggesting very strong cooling in the post-shock wind collision region. As such this system is more difficult to simulate, as a higher resolution and lower Courant number are required in order to reliably simulate the post-shock cooling effect. The orbital and wind parameters of this system were derived from Soulain et al., 2018 and Harries et al., 2004.

WR 140 was simulated for this experiment as it represents an archetypical episodic CWB system, whose infrared dust emission peaks around periastron passage. WR 140 deviates from WR 98a and WR 104 by being extremely eccentric, which significantly effects the cooling parameter as the orbit progresses (figure 5.2). Additionally, the minimum value for χ is significantly larger than the other systems, and hence cooling would be less dominant on the dynamics of the

5. HYDRODYNAMICAL SIMULATIONS OF WCD SYSTEMS

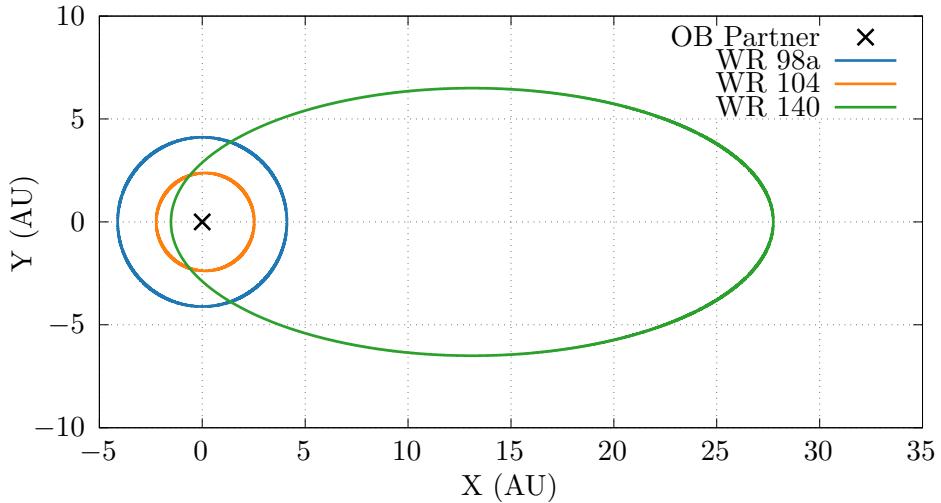


Figure 5.1: Orbital paths for each system, a co-ordinate transform is applied such that the orbitally dominant OB partner is always at co-ordinate (0,0). WR 140 has a significantly more eccentric orbit, as well as a much longer orbital period.

WCR, even at periaxis. Though these simulations do not calculate wind acceleration due to radiative line driving, both stellar winds are expected to be accelerated close to their terminal wind velocities (Lamers & Cassinelli, 1999). However, this discrepancy should be noted when considering the results of this paper. The orbital and wind parameters of this system were derived from work by Monnier et al., 2011, Usov, 1991, as well as Thomas et al., 2021.

5.2.4 Radiative transfer modelling

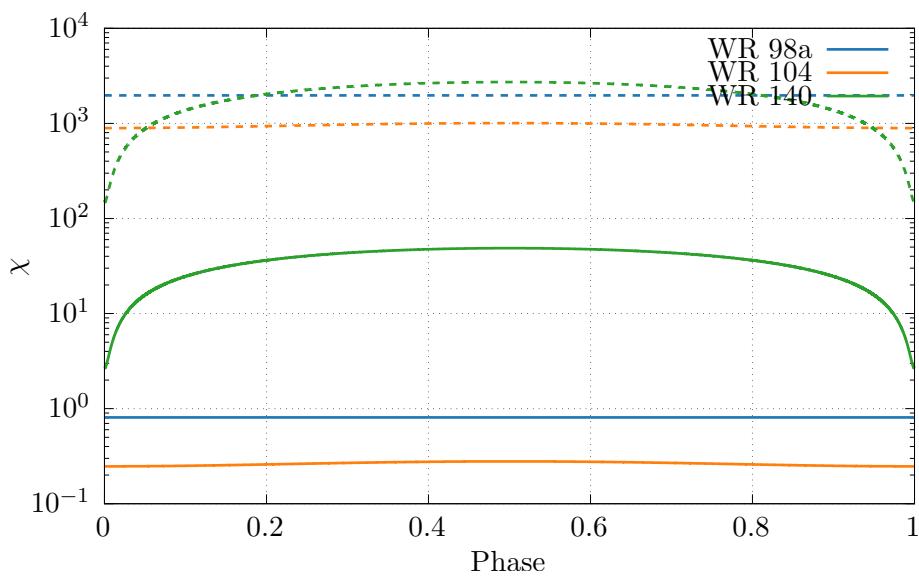


Figure 5.2: Change in WR cooling parameter χ over a single orbit, solid lines represent the primary WC star, while dashed lines represent their OB partners. The dynamics of the WCR for WR 98a and WR 104 is dominated by cooling throughout their entire orbits, while WR 140 is adiabatic for most of its orbit. Additionally OB stars have significantly higher cooling parameters, and thus their flows behave adiabatically.

5. HYDRODYNAMICAL SIMULATIONS OF WCD SYSTEMS

CHAPTER 6

An Exploration on the Influence of Wind Velocity of
Dust formation in WCd Systems

6. INFLUENCE OF WIND VELOCITY ON DUST FORMATION

6.1 Introduction

6.2 Methodology

6.3 Model Parameters

6.4 Results

6.4 Results

Model	v_{WR}^{∞} cm s $^{-1}$	v_{OB}^{∞} cm s $^{-1}$	η	χ_{WR}	χ_{OB}
sim-1-wr	2.00×10^8	2.00×10^8	0.010	19.149	1915
sim-2-wr	1.36×10^8	2.00×10^8	0.015	4.060	1915
sim-3-wr	1.03×10^8	2.00×10^8	0.019	1.332	1915
sim-4-wr	8.26×10^7	2.00×10^8	0.024	0.557	1915
sim-5-wr	6.91×10^7	2.00×10^8	0.029	0.273	1915
sim-6-wr	5.94×10^7	2.00×10^8	0.034	0.149	1915
sim-7-wr	5.21×10^7	2.00×10^8	0.038	0.088	1915
sim-8-wr	4.63×10^7	2.00×10^8	0.043	0.055	1915
sim-9-wr	4.18×10^7	2.00×10^8	0.048	0.036	1915
sim-10-wr	3.80×10^7	2.00×10^8	0.053	0.025	1915
sim-11-wr	3.49×10^7	2.00×10^8	0.057	0.018	1915
sim-12-wr	3.22×10^7	2.00×10^8	0.062	0.013	1915
sim-13-wr	2.99×10^7	2.00×10^8	0.067	0.010	1915
sim-14-wr	2.79×10^7	2.00×10^8	0.072	0.007	1915
sim-15-wr	2.62×10^7	2.00×10^8	0.076	0.006	1915
sim-16-wr	2.47×10^7	2.00×10^8	0.081	0.004	1915
sim-17-wr	2.33×10^7	2.00×10^8	0.086	0.004	1915
sim-18-wr	2.21×10^7	2.00×10^8	0.091	0.003	1915
sim-19-wr	2.10×10^7	2.00×10^8	0.095	0.002	1915
sim-20-wr	2.00×10^7	2.00×10^8	0.100	0.002	1915

Table 6.1: WR parameters

6. INFLUENCE OF WIND VELOCITY ON DUST FORMATION

Model	v_{WR}^{∞} cm s $^{-1}$	v_{OB}^{∞} cm s $^{-1}$	η	χ_{WR}	χ_{OB}
sim-1-ob	1.00×10^8	1.00×10^8	0.010	1.197	120
sim-2-ob	1.00×10^8	1.47×10^8	0.015	1.197	564
sim-3-ob	1.00×10^8	1.95×10^8	0.019	1.197	1721
sim-4-ob	1.00×10^8	2.42×10^8	0.024	1.197	4112
sim-5-ob	1.00×10^8	2.89×10^8	0.029	1.197	8403
sim-6-ob	1.00×10^8	3.37×10^8	0.034	1.197	15407
sim-7-ob	1.00×10^8	3.84×10^8	0.038	1.197	26079
sim-8-ob	1.00×10^8	4.32×10^8	0.043	1.197	41520
sim-9-ob	1.00×10^8	4.79×10^8	0.048	1.197	62975
sim-10-ob	1.00×10^8	5.26×10^8	0.053	1.197	91833
sim-11-ob	1.00×10^8	5.74×10^8	0.057	1.197	129630
sim-12-ob	1.00×10^8	6.21×10^8	0.062	1.197	178045
sim-13-ob	1.00×10^8	6.68×10^8	0.067	1.197	238900
sim-14-ob	1.00×10^8	7.16×10^8	0.072	1.197	314164
sim-15-ob	1.00×10^8	7.63×10^8	0.076	1.197	405950
sim-16-ob	1.00×10^8	8.11×10^8	0.081	1.197	516516
sim-17-ob	1.00×10^8	8.58×10^8	0.086	1.197	648263
sim-18-ob	1.00×10^8	9.05×10^8	0.091	1.197	803739
sim-19-ob	1.00×10^8	9.53×10^8	0.095	1.197	985633
sim-20-ob	1.00×10^8	1.00×10^9	0.100	1.197	1196783

Table 6.2: OB parameters

CHAPTER 7

Final Notes and Conclusions

7. FINAL NOTES AND CONCLUSIONS

7.1 Conclusions

7.1.1 Causes of dust formation in WCB systems

7.1.2 The role of eccentricity in dust formation

7.2 Future Study

7.2.1 More complex models

7.2.2 Further simulations of observed systems

7.2.3 Radiative transfer

7.2.4 WR+WR systems

7.2.5 Next generation telescopes

7.3 Other Observations

7.3.1 *Doctorate Strangelove or: How I Learned to Stop Worrying and Love Numerics*

7.3.2 Join the physics department, see the world

7.3.3 Paul Erdős was probably onto something

7.3.4 Carinae Strain: PhD research in a time of pandemic

7.3.5 WR 104 as a local GRB candidate

APPENDIX A

Astrophysical Shocks

A. ASTROPHYSICAL SHOCKS

APPENDIX B

Software Carpentry

B. SOFTWARE CARPENTRY

B.1 Amdahl's Law

B.2 Version Control

BIBLIOGRAPHY

Book Sources

- Carroll, B. W. & Ostlie, D. A. (2014). *An Introduction to Modern Astrophysics* (Second international). Pearson
OCLC: 868368508.
- Dyson, J. E. (2021). *The physics of the interstellar medium* (Third edition.). CRC Press.
- Lamers, H. J. & Cassinelli, J. P. (1999). *Introduction to stellar winds*. Cambridge University Press.
- Oswalt, T. D. & Barstow, M. A. (Eds.). (2013). *Planets, Stars and Stellar Systems*. Springer Netherlands. <https://doi.org/10.1007/978-94-007-5615-1>
- Ryan, S. G. & Norton, A. J. (2010). *Stellar evolution and nucleosynthesis*. Cambridge University Press
OCLC: ocn437083016.
- Rybicki, G. B. & Lightman, A. P. (2004). *Radiative processes in astrophysics*. Wiley
OCLC: 255501661.
- Salaris, M. & Cassisi, S. (2005). *Evolution of Stars and Stellar Populations*.
- Spitzer Jr., L. (2008, November 20). *Physical Processes in the Interstellar Medium*. John Wiley & Sons.
- Vink, J. S. (Ed.). (2015). *Very Massive Stars in the Local Universe* (Vol. 412). Springer International Publishing. <https://doi.org/10.1007/978-3-319-09596-7>
- Ward-Thompson, D. & Whitworth, A. P. (2011). *An Introduction to Star Formation*. Cambridge University Press. <https://doi.org/10.1017/CBO9780511974021>

BIBLIOGRAPHY

Journal Sources

- Allen, D. A., Swings, J. P. & Harvey, P. M. (1972). Infrared photometry of northern Wolf-Rayet stars. *Astronomy and Astrophysics*, 20, 333–336.
- Castor, J. I., Abbott, D. C. & Klein, R. I. (1975). Radiation-driven winds in Of stars. *The Astrophysical Journal*, 195, 157. <https://doi.org/10.1086/153315>
- Cherepashchuk, A. M. (1976). Detectability of Wolf-Rayet binaries from X-rays. *Soviet Astronomy Letters*, 2, 138.
- Crowther, P. A. (2003). Dust Formation around Wolf-Rayet Stars. *Astrophysics and Space Science*, 285(3), 677–685. <https://doi.org/10.1023/A:1026157126395>
- Crowther, P. A. (2007). Physical Properties of Wolf-Rayet Stars. *Annual Review of Astronomy and Astrophysics*, 45(1), 177–219. <https://doi.org/10.1146/annurev.astro.45.051806.110615>
- Draine, B. & Salpeter, E. (1979). Destruction mechanisms for interstellar dust. *The Astrophysical Journal*, 231, 438–455.
- Dwek, E. & Werner, M. W. (1981). The Infrared Emission From Supernova Condensates. *The Astrophysical Journal*, 248, 138. <https://doi.org/10.1086/159138>
- Eichler, D. & Usov, V. (1993). Particle acceleration and nonthermal radio emission in binaries of early-type stars. *The Astrophysical Journal*, 402, 271–279. <https://doi.org/10.1086/172130>
- Gottlieb, S., Ketcheson, D. I. & Shu, C.-W. (2009). High Order Strong Stability Preserving Time Discretizations. *Journal of Scientific Computing*, 38(3), 251–289. <https://doi.org/10.1007/s10915-008-9239-z>
- Grimaldo, E., Reimer, A., Kissmann, R., Niederwanger, F. & Reitberger, K. (2019). Proton Acceleration in Colliding Stellar Wind Binaries. *The Astrophysical Journal*, 871, 55. <https://doi.org/10.3847/1538-4357/aaf6ee>
- Harries, T. J., Monnier, J. D., Symington, N. H. & Kurosawa, R. (2004). Three-dimensional dust radiative-transfer models: The Pinwheel Nebula of WR 104. *Monthly Notices of the Royal Astronomical Society*, 350(2), 565–574. <https://doi.org/10.1111/j.1365-2966.2004.07668.x>
- Hendrix, T., Keppens, R., van Marle, A. J., Camps, P., Baes, M. & Meliani, Z. (2016). Pinwheels in the sky, with dust: 3D modelling of the Wolf-Rayet 98a environment. *Monthly Notices of the Royal Astronomical Society*, 460(4), 3975–3991. <https://doi.org/10.1093/mnras/stw1289>

JOURNAL SOURCES

- Le Teuff, Y. H. (2002). A Model of Dust Formation in Clumpy Wolf-Rayet Winds. *260*, 223.
- Lucy, L. B. & Solomon, P. M. (1970). Mass Loss by Hot Stars. *The Astrophysical Journal*, *159*, 879. <https://doi.org/10.1086/150365>
- Marchenko, S. V., Moffat, A. F. J. & Crowther, P. A. (2010). Population I Wolf-Rayet Runaway Stars: The Case of WR124 and its Expanding Nebula M1-67. *The Astrophysical Journal*, *724*, L90–L94. <https://doi.org/10.1088/2041-8205/724/1/L90>
ADS Bibcode: 2010ApJ...724L..90M
- Monnier, J. D., Zhao, M., Pedretti, E., Millan-Gabet, R., Berger, J.-P., Traub, W., Schloerb, F. P., ten Brummelaar, T., McAlister, H., Ridgway, S., Sturmann, L., Sturmann, J., Turner, N., Baron, F., Kraus, S., Tannirkulam, A. & Williams, P. M. (2011). First Visual Orbit for the Prototypical Colliding-wind Binary WR 140. *The Astrophysical Journal Letters*, *742*, L1. <https://doi.org/10.1088/2041-8205/742/1/L1>
- Nazé, Y., Koenigsberger, G., Pittard, J. M., Parkin, E. R., Rauw, G., Corcoran, M. F. & Hillier, D. J. (2018). A Changing Wind Collision. *The Astrophysical Journal*, *853*(2), 164. <https://doi.org/10.3847/1538-4357/aaa29c>
- Neugent, K. & Massey, P. (2019). The Wolf-Rayet Content of the Galaxies of the Local Group and Beyond. *Galaxies*, *7*(3), 74. <https://doi.org/10.3390/galaxies7030074>
- Pauldrach, A., Pittard, J. M. & Kudritzki, R. P. (1986). Radiation-driven winds of hot luminous stars. Improvements of the theory and first results. *Astronomy and Astrophysics*, Vol. *164*, p. 86-100 (1986), *164*, 86.
- Pittard, J. M. (2009). 3D models of radiatively driven colliding winds in massive O+O star binaries - I. Hydrodynamics. *Monthly Notices of the Royal Astronomical Society*, *396*(3), 1743–1763. <https://doi.org/10.1111/j.1365-2966.2009.14857.x>
- Pittard, J. M. & Dawson, B. (2018). Colliding stellar winds structure and X-ray emission. *Monthly Notices of the Royal Astronomical Society*, *477*(4), 5640–5645. <https://doi.org/10.1093/mnras/sty1025>
- Prilutskii, O. F. & Usov, V. V. (1976). X rays from Wolf-Rayet binaries. *Soviet Astronomy*, *20*, 2.
- Rosslowe, C. K. & Crowther, P. A. (2015). Spatial distribution of Galactic Wolf-Rayet stars and implications for the global population. *Monthly Notices of the Royal Astronomical Society*, *447*(3), 2322–2347. <https://doi.org/10.1093/mnras/stu2525>

BIBLIOGRAPHY

- Schure, K. M., Kosenko, D., Kaastra, J. S., Keppens, R. & Vink, J. (2009). A New Radiative Cooling Curve Based on an Up-To-Date Plasma Emission Code. *Astronomy & Astrophysics*, 508(2), 751–757. <https://doi.org/10.1051/0004-6361/200912495>
- Soulain, A., Millour, F., Lopez, B., Matter, A., Lagadec, E., Carbillet, M., Camera, A., Lamberts, A., Langlois, M., Milli, J., Avenhaus, H., Magnard, Y., Roux, A., Moulin, T., Carle, M., Sevin, A., Martinez, P., Abe, L. & Ramos, J. (2018, June 22). *The SPHERE view of Wolf-Rayet 104*. arXiv: 1806.08525 [astro-ph]. Retrieved October 23, 2018, from <http://arxiv.org/abs/1806.08525>
- Spiteri, R. J. & Ruuth, S. J. (2002). A New Class of Optimal High-Order Strong-Stability-Preserving Time Discretization Methods. *SIAM Journal on Numerical Analysis*, 40(2), 469–491. <https://doi.org/10.1137/S0036142901389025>
- Stevens, I. R., Blondin, J. M. & Pollock, A. M. T. (1992). Colliding winds from early-type stars in binary systems. *The Astrophysical Journal*, 386, 265–287. <https://doi.org/10.1086/171013>
- Stone, J. M., Tomida, K., White, C. J. & Felker, K. G. (2020). The Athena++ Adaptive Mesh Refinement Framework: Design and Magnetohydrodynamic Solvers. *The Astrophysical Journal Supplement Series*, 249(1), 4. <https://doi.org/10.3847/1538-4365/ab929b>
- Thomas, J. D., Richardson, N. D., Eldridge, J. J., Schaefer, G. H., Monnier, J. D., Sana, H., Moffat, A. F. J., Williams, P., Corcoran, M. F., Stevens, I. R., Weigelt, G., Zainol, F. D., Anugu, N., Le Bouquin, J.-B., ten Brummelaar, T., Campos, F., Couperus, A., Davies, C. L., Ennis, J., ... Zurmühl, U. (2021). The orbit and stellar masses of the archetype colliding-wind binary WR 140. *Monthly Notices of the Royal Astronomical Society*, 504(4), 5221–5230. <https://doi.org/10.1093/mnras/stab1181>
- Townsend, R. H. D. (2009). An Exact Integration Scheme for Radiative Cooling in Hydrodynamical Simulations. *The Astrophysical Journal Supplement Series*, 181(2), 391–397. <https://doi.org/10.1088/0067-0049/181/2/391>
- Usov, V. V. (1991). Stellar wind collision and dust formation in long-period, heavily interacting Wolf-Rayet binaries. *Monthly Notices of the Royal Astronomical Society*, 252(1), 49–52. <https://doi.org/10.1093/mnras/252.1.49>
- Williams, P. M. (2008). Dust formation by colliding-wind binaries. 33, 71–76.
- Williams, P. M., Marchenko, S. V., Marston, A. P., Moffat, A. F. J., Varricatt, W. P., Dougherty, S. M., Kidger, M. R., Morbidelli, L. & Tapia, M. (2009). Orbitally modulated dust formation by the WC7+O5 colliding-wind binary WR 140. *Monthly Notices of the Royal*

JOURNAL SOURCES

Astronomical Society, 395(3), 1749–1767. <https://doi.org/10.1111/j.1365-2966.2009.14664.x>

Williams, P. M. & van der Hucht, K. A. (2015). The colliding-wind WC9+OB system WR 65 and dust formation by WR stars, 275–278.

Williams, P. M., van der Hucht, K. A., Thé, P. S. & Bouchet, P. (1990). A Dust Shell around the Early Type Wolf-Rayet Star WR:19. *Monthly Notices of the Royal Astronomical Society*, 247, 18P.

Zubko, V. G. (1998). On the physical model of dust around Wolf-Rayet stars. *Monthly Notices of the Royal Astronomical Society*, 295(1), 109–118. <https://doi.org/10.1046/j.1365-8711.1998.29511348.x>